

Chapter 11

The thermohaline circulation of the ocean

The ‘thermohaline circulation’ is that part of the ocean circulation induced by deep-reaching convection driven by surface buoyancy loss in polar latitudes, as sketched schematically in Fig.11.1¹. As we shall see, deep convection in the ocean is highly localized in space and only occurs in a few key locations; in particular, the northern North Atlantic and around Antarctica. However, the response of the ocean to this localized forcing is global in scale. Giant patterns of meridional overturning circulation are set up that cross the equator and connect the hemispheres together. Unlike the faster wind-driven circulation, which is confined to the top kilometer or so, the thermohaline circulation plays a major role in setting properties of the abyssal ocean. Both wind-driven (Chapter 10) and buoyancy-driven circulations play an important role in meridional ocean heat transport. However, because of the very long timescales and very weak currents involved, the thermohaline circulation is much less well observed or understood. We shall see that theory has played a central role in shaping our conception of the likely circulation patterns and mechanisms.

In this Chapter, then, we describe the patterns of air-sea heat and fresh water fluxes that drive the thermohaline circulation and go on to discuss

¹The phrase ‘thermohaline circulation’ is widely used but not precisely defined. It means different things to different people. Perhaps its most literal interpretation is the circulation of heat and salt in the ocean and thus involves both wind-driven and buoyancy driven circulation. Here, however, we adopt its more common, narrow usage, to mean the circulation induced by polar convection.

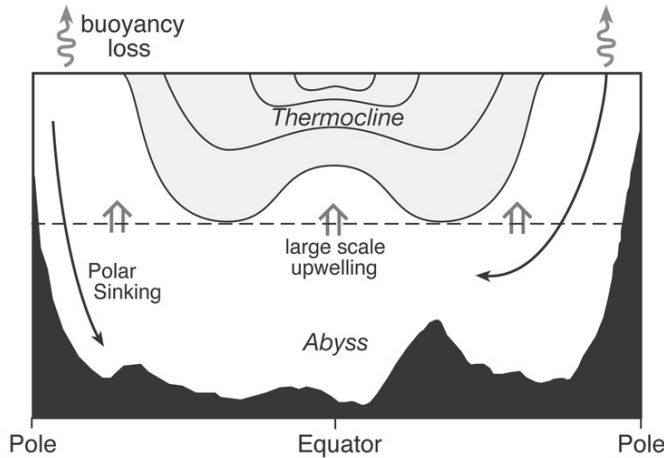


Figure 11.1: The deep ocean is ventilated by localized convection at polar latitudes, induced by loss of buoyancy (due to cooling and/or salt input) causing surface waters to sink to depth. Compensating upwelling is thought to occur on the large-scale, as indicated by the vertical arrows at mid-depth.

inferences of abyssal flow patterns and rates from observations of interior tracer distributions such as salinity and oxygen. We then develop a simple conceptual model and associated laboratory experiments of the thermohaline circulation employing the same dynamical framework — Taylor-Proudman on the sphere — used to discuss the wind-driven circulation in Chapter 10. This model predicts the existence of deep western boundary currents carrying fluid away from their source regions whose existence is confirmed by observations. Finally we discuss the role of the wind-driven and thermohaline circulations in the meridional flux of heat and freshwater.

11.1 Air-sea fluxes and surface property distributions

11.1.1 Heat, freshwater and buoyancy fluxes

Atmospheric convection is triggered by warming at the surface: vertical mass transport is confined to a few regions of strong updrafts driven by deep convection over the warmest oceans and land masses in the tropics, with broader

areas of subsidence in between — see the atmospheric mean meridional circulation plotted in Fig.5.21. In contrast to the atmosphere, the ocean is forced from above by air-sea fluxes. We therefore expect ocean convection to be most prevalent in the *coldest* regions where the interior stratification is small, most likely at high latitudes in winter where surface density can increase through:

1. direct cooling, reducing temperature and hence increasing density,
2. brine rejection in ice formation, thus increasing salinity (and hence density) of the water immediately below the ice.

Whether a parcel of water sinks depends on its buoyancy anomaly (as described in Section 4.2.1) defined by Eq.(4.3) which we write out again here adopting our oceanographic notation:

$$b = -g \frac{(\sigma - \sigma_o)}{\rho_{ref}} \quad (11.1)$$

where g is the acceleration due to gravity and $\sigma - \sigma_o$ is the difference between the density of the parcel and its surroundings (see Eq.9.5). As discussed in Section 9.1.3, the buoyancy of sea-water at the surface depends on both the T and S distribution. To determine whether convection will occur we must therefore consider both the flux of heat and freshwater across the ocean surface which induce T , S and hence buoyancy changes, as well as the ambient, pre-existing stratification of the water column.

The equations governing the evolution of T and S are:

$$\frac{DT}{Dt} = -\frac{1}{\rho_{ref} c_w} \frac{\partial Q}{\partial z} \quad (11.2)$$

$$\frac{DS}{Dt} = S \frac{\partial E}{\partial z} \quad (11.3)$$

where c_w is the heat capacity of water (see Table 9.3) and Q and E are, respectively, the turbulent vertical flux of heat and freshwater driven by air-sea exchange, convection, ice formation and vertical mixing in the ocean (as sketched schematically in Fig.9.11). At the surface $Q = Q_{\text{net}}$, the net heat flux across the sea surface (see Eq.11.5 below) and $E = E_{\text{surface}} = E - P$ (evaporation minus precipitation, including that due to river run-off and ice formation processes) is the net fresh water flux across the sea surface.

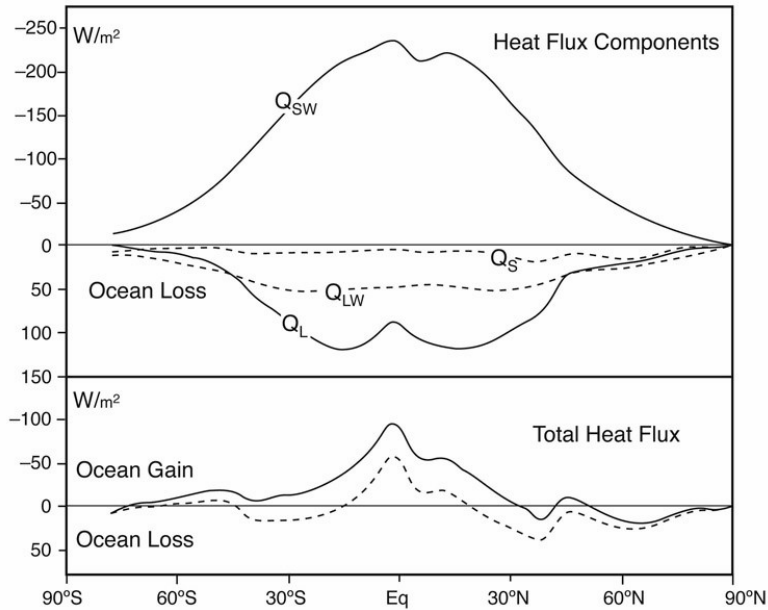


Figure 11.2: Upper: Zonal averages of heat transfer to the ocean by insolation Q_{SW} , and loss by longwave radiation Q_{LW} , sensible heat flux Q_S , and latent heat flux Q_L , calculated by DaSilva, Young, and Levitus (1995) using the COADS data set. Lower: Net heat flux through the sea surface calculated from the data above (solid line) and net heat flux constrained to give heat and fresh-water transports by the ocean that match independent calculations of these transports. The area under the lower curves ought to be zero, but it is 16 W m^{-2} for the unconstrained case (solid line) and -3 W m^{-2} for the constrained case (dotted line). From Robert H. Stewart.

Typically \mathcal{Q} and \mathcal{E} decay with depth over the mixed layer from these surface values. Note that the minus sign in Eq.(11.2) ensures that if heat is lost from the ocean ($\mathcal{Q}_{\text{net}} > 0$), its temperature decreases.

The buoyancy equation can be deduced by taking $\frac{D}{Dt}$ of Eq.(11.1) and using Eqs.(9.5), (11.2) and (11.3) to obtain

$$\begin{aligned}\frac{Db}{Dt} &= -\frac{g}{\rho_{\text{ref}}} \left[\frac{\alpha_T}{c_w} \frac{\partial Q}{\partial z} + \rho_{\text{ref}} \beta_S S \frac{\partial \mathcal{E}}{\partial z} \right] \\ &= -\frac{\partial B}{\partial z},\end{aligned}$$

where B is the vertical buoyancy flux, allowing us to identify the air-sea buoyancy flux thus:

$$B_{\text{surface}} = \frac{g}{\rho_{\text{ref}}} \left(\underbrace{\frac{\alpha_T}{c_w} \mathcal{Q}_{\text{net}}}_{\text{thermal}} + \underbrace{\rho_{\text{ref}} \beta_S S (E - P)}_{\text{haline}} \right) \quad (11.4)$$

where α_T , β_S are defined in Eqs.(9.3) and (9.4), respectively. The units of buoyancy flux are $\text{m}^2 \text{s}^{-3}$, that of velocity \times acceleration. We see that the buoyancy flux is made up of both thermal and haline components.

The net heat flux through the sea surface is itself made up of a number of components:

$$\mathcal{Q}_{\text{net}} = \underbrace{\mathcal{Q}_{SW}}_{\text{shortwave}} + \underbrace{\mathcal{Q}_{LW}}_{\text{longwave}} + \underbrace{\mathcal{Q}_S}_{\text{sensible flux}} + \underbrace{\mathcal{Q}_L}_{\text{latent flux}} \quad (11.5)$$

Estimates of the various terms from observations are shown in Figs.11.2, 11.3 and 11.4. The units are in W m^{-2} .

The shortwave flux is the incoming solar radiation that reaches the sea surface and penetrates the ocean (the ocean has a low albedo — see Table 2.2), warming it down to a depth of 100 – 200 meters, depending on the transparency of the water. The longwave flux is the net flux of longwave radiation at the sea surface due to the radiation beamed out by the ocean according to the blackbody law, Eq.(2.2), less the ‘back radiation’ from the atmospheric cloud and water vapor layer (see Chapter 2).

The sensible heat flux is the flux of heat through the sea surface due to turbulent exchange. It depends on the wind speed and the air-sea temperature difference according to the following (approximate) formula:

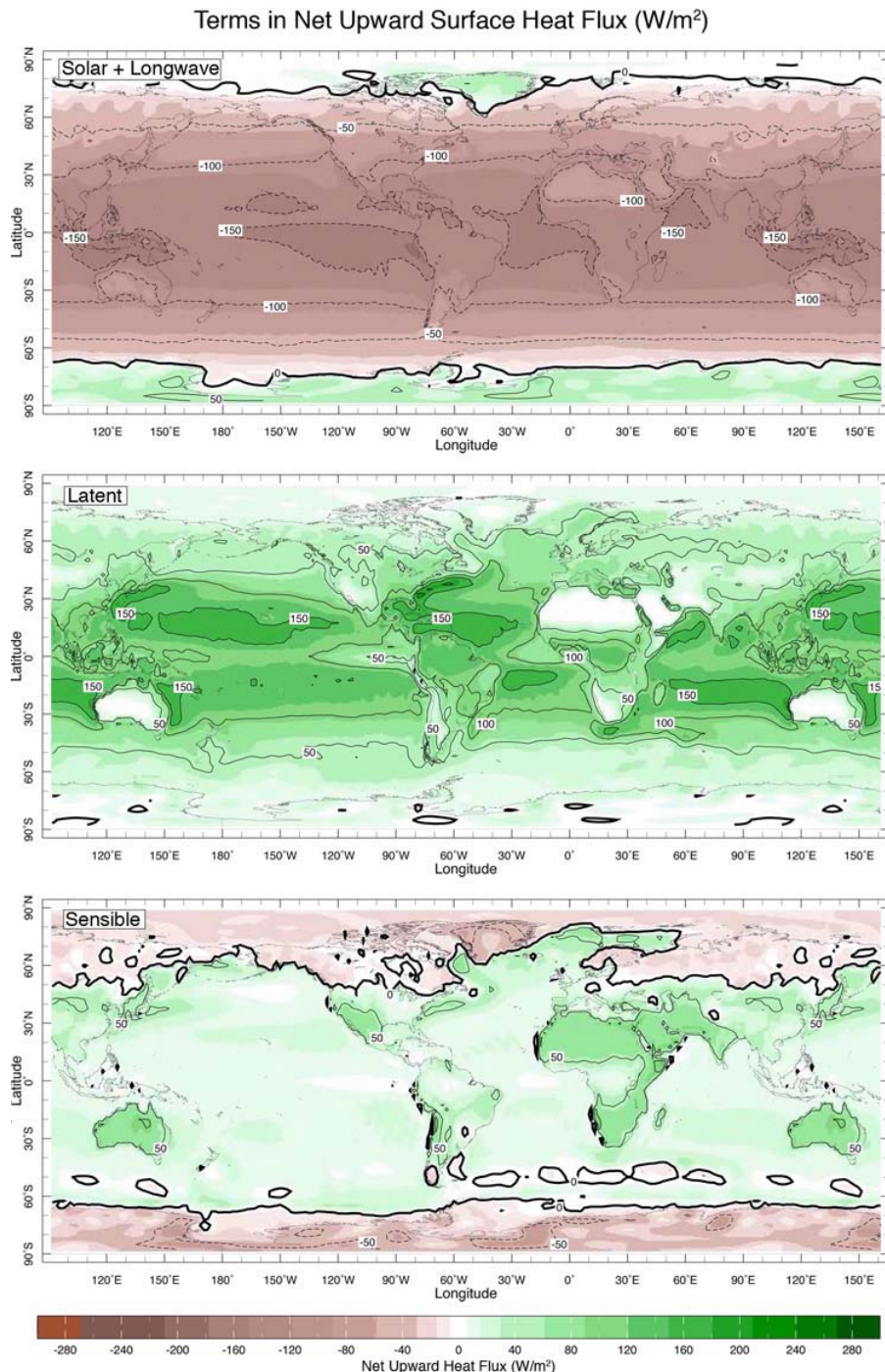


Figure 11.3: Global map of $Q_{SW} + Q_{LW}$, Q_L and Q_S across the sea surface in W m^{-2} . Areas in which the fluxes are upward, in to the atmosphere, are positive and shaded green; areas in which the flux is downward, in to the ocean, are negative and shaded brown. Contour interval is 50 W m^{-2} . From Kalnay et.al. 1996.

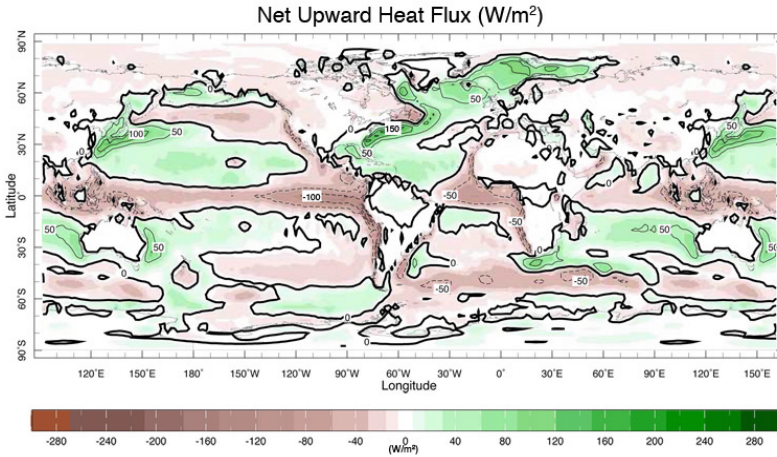


Figure 11.4: Global map of net annual-mean, constrained, heat flux, \mathcal{Q}_{net} , across the sea surface in Wm^{-2} . Areas in which the fluxes are upward, in to the atmosphere, are shaded green; areas in which the flux is downward, in to the ocean, are shaded brown. Contour interval is 50 Wm^{-2} . From Kalnay et.al. 1996.

$$\mathcal{Q}_S = \rho_{\text{air}} c_p c_S u_{10} (SST - T_{\text{air}}) \quad (11.6)$$

where ρ_{air} is the density of air at the surface, c_S is a stability-dependent bulk transfer coefficients for heat (which typically has a value of about 10^{-3}), c_p is the specific heat of air, T_{air} and u_{10} are, respectively, the air temperature and wind speed at a height of 10 m and SST is the sea surface temperature. Note that if $SST > T_{\text{air}}$, $\mathcal{Q}_S > 0$ and the sensible heat flux is out of the ocean which therefore cools. The global average temperature of the surface ocean is indeed 1 or 2 degrees warmer than the atmosphere and so, on the average, sensible heat is transferred from the ocean to the atmosphere; see the zonal-average curves in Fig.11.2.

The latent heat flux is the flux of heat carried by evaporated water. The water vapor leaving the ocean eventually condenses into water droplets forming clouds — as described in Chapter 4 and sketched in Fig.11.5 — releasing its latent heat of vaporization to the atmosphere. The latent heat flux depends on the wind-speed and relative humidity according to, analogously to Eq.(11.6),

$$\mathcal{Q}_L = \rho_{air} L_e c_L u_{10} (q_*(SST) - q_{air}) \quad (11.7)$$

where c_L is a stability-dependent bulk transfer coefficients for water vapor (which, like c_S in Eq.(11.6), typically has a value $\sim 10^{-3}$), L_e is the latent heat of evaporation, q_{air} is the specific humidity (in kg vapor per kg air) and q_* is the specific humidity at saturation which depends on SST (see Section 4.5.1). High winds and dry air evaporate much more water than weak winds and moist air. Evaporative energy loss rises steeply with water temperature due to the sensitivity of saturation vapor pressure to temperature — see Fig.1.5 — and the concomitant increase in vapor density gradient between the sea and air. At higher latitudes where these gradients are smaller, evaporative transfer is of lesser importance and sensible heat transfer, which can be of either sign, becomes more important (see Fig.11.3).

It is very difficult to directly measure the terms that make up Eq.(11.5). Estimates can be made by combining in-situ measurements (when available), satellite observations and the output of numerical models constrained by observations. Zonal-average estimates of each term in Eq.(11.5) are shown in Fig.11.2. We see that \mathcal{Q}_{SW} peaks in the tropics and is somewhat balanced by the evaporative processes \mathcal{Q}_L and outgoing longwave radiation, \mathcal{Q}_{LW} , with \mathcal{Q}_S making only a small contribution. Note that solar radiation is the only term that warms the ocean. The major source of cooling is \mathcal{Q}_L . Its typical magnitude can be estimated by noting that the net upward transfer of H₂O in evaporation must equal precipitation (see Fig.11.5). This suggests that the upward flux of energy in latent form is:

$$\mathcal{Q}_L \sim L_e \frac{dm}{dt}$$

where L_e is the latent heat of evaporation and m is the mass of water falling per square metre (note that the precipitation rate $P = \frac{1}{\rho_{ref}} \frac{dm}{dt}$ and has units of velocity, most often expressed in meters per year). Inserting numerical values from Table 9.3 the above yields 71 W m⁻² for every m y⁻¹ of rainfall. This is broadly in accord with Fig.11.2 since the annual mean rainfall rate is around 1 m y⁻¹.

Note that if the ocean is not to warm up or cool down in the long-run, the net air-sea heat flux integrated over the surface of the ocean, the area beneath the continuous black line in the lower panel in Fig.11.2, should be zero. In fact, due to uncertainties in the data, it is 16 W m⁻². That this is an

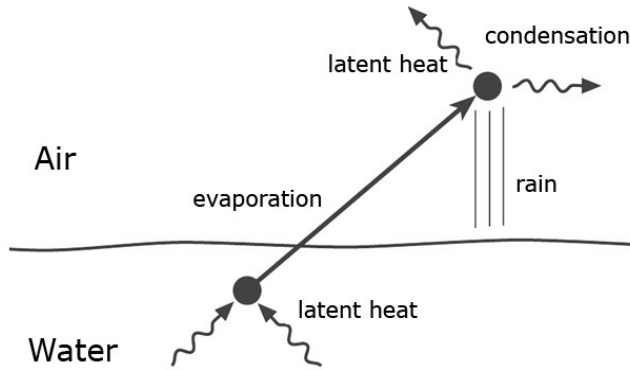


Figure 11.5: Latent heat is taken from the ocean to evaporate water that is subsequently released to the atmosphere when the vapor condenses to form rain.

unrealistically large net flux can easily be deduced as follows. If the global ocean were heated by an air-sea flux of magnitude Q_{net} to a depth h over a time Δt , it would warm (assuming it to be well-mixed) by an amount ΔT given by, see Eq.(11.2):

$$\Delta T = \frac{Q_{\text{net}} \Delta t}{h \rho_{\text{ref}} c_w}$$

or 0.75°C for every 1 W m^{-2} of global imbalance sustained for a 100 year period, assuming $h = 1 \text{ km}$, and the data in Table 9.3. This is a full 12°C if the imbalance is 16 W m^{-2} ! The ‘observed’ warming of the ocean’s thermocline during the second half of the 20th century is an almost imperceptible few tenths of a $^{\circ}\text{C}$. Clearly Q_{net} integrated over the global ocean must, in reality, be very close to zero. Thus, in the lower panel of Fig.11.2, a constrained (adjusted) zonal-average estimate of Q_{net} is shown by the dotted line, the area under which is close to zero. This is much the more likely distribution. We now see that the ocean gains heat in the tropics and loses it at high latitudes, as seems intuitively reasonable.

The geographical distribution of Q_{net} and $E - P$ are shown in Figs.11.4 and 11.6. Both fields are constrained to have near-zero global integral. We generally see cooling of the oceans in the northern subtropics and high latitudes, and particularly intense regions of cooling over the Kuroshio and Gulf Stream extensions, exceeding 100 W m^{-2} in the annual mean. These latter

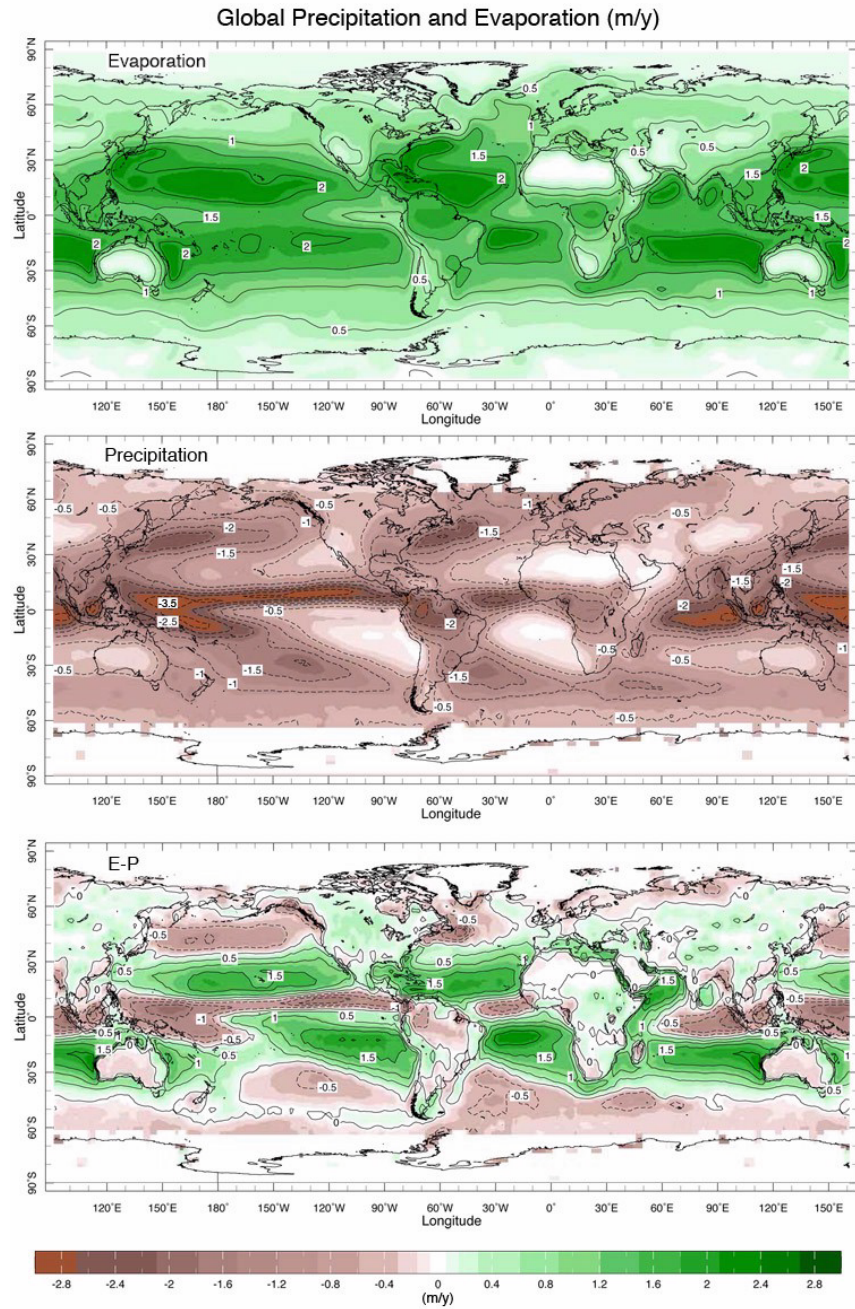


Figure 11.6: A map of annual-mean evaporation (E), precipitation (P) and evaporation minus precipitation ($E - P$) over the globe. In the bottom map, $E > P$ over the green areas; $P > E$ over the brown areas. The contour interval is 0.5 m y^{-1} . From Kalnay et.al. 1996.

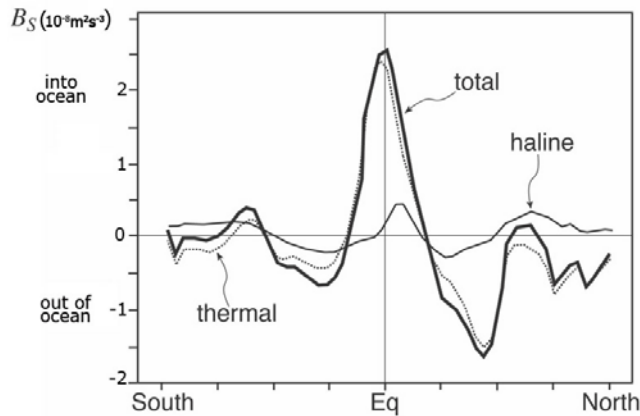


Figure 11.7: The zonally-averaged buoyancy forcing (thick black line) and the thermal (dotted line) and haline (thin line) components that make it up — Eq.(11.4) in units of $\text{m}^2 \text{s}^{-3}$, courtesy of Arnaud Czaja. Note that a heat flux of 50W m^{-2} is (roughly) equal to a buoyancy flux of $2 \times 10^{-8} \text{m}^2 \text{s}^{-3}$. Data from Kalnay et.al (1996).

regions are places where, in winter, very cold air blows over the ocean from the adjacent cold land-masses and where the western boundary currents of the ocean carry warm fluid from the tropics to higher latitudes. Such intense regions of heat loss are not seen in the southern hemisphere because the juxtaposition of land and sea is largely absent. Moreover, because the ‘fetch’ of ocean is so much larger there, the air-sea temperature difference and hence air-sea flux is much reduced. In the tropics we observe warming of the ocean due to incoming shortwave solar radiation.

The pattern of $E - P$, Fig.11.6, shows excess of evaporation over precipitation in the subtropics, creating the region of high salinity seen in Fig.9.4. Precipitation exceeds evaporation in the tropics (in the rising branch of the Hadley circulation), and also in high latitudes. This creates anomalously fresh surface water (cf. see Fig.9.4) and acts to stabilize the water column.

Another perspective on the forcing of thermohaline circulation is given by Fig.11.7 which shows the zonally-averaged air-sea buoyancy flux B_{surface} defined by Eq.(11.4), and the thermal and haline components that make it up. Buoyancy loss from the ocean peaks in the subtropics, yet we do not observe deep mixed layers at these latitudes — see Fig.9.10. Evidently here

buoyancy loss is not strong enough to ‘punch through’ the strong stratification of the main thermocline (cf. Fig.9.7). It is clear from Fig.11.7 that the haline component stabilizes the polar oceans (excess of precipitation over evaporation at high latitudes), but is generally considerably weaker in magnitude than the thermal contribution to the buoyancy flux. Nevertheless, in the present climate, the weak stratification of the polar oceans enables the buoyancy lost there to trigger deep-reaching convection which ventilates the abyssal ocean. In past climates it is thought that the freshwater supply to the polar oceans may have been different (due, for example, to enhanced atmospheric moisture transport in a warm climate or melting of polar ice releasing fresh water) and could be an important driver of climate variability (see Section 12.3.5).

Finally we note that Figs.11.4, 11.6 and 11.7 only show components of the buoyancy flux associated with air-sea exchange — they ignore the effects of, for example, brine rejection in ice formation which is thought to be a key mechanism in the creation of dense water around Antarctica. Here ice is blown northwards in the surface Ekman layers (to the left of the wind in the southern hemisphere) leaving salty and hence dense water behind, which is susceptible to convection.²

11.1.2 Interpretation of surface temperature distributions

The observed SST distribution shown in Figs.9.3, 9.14, 9.15 and 9.16 is maintained by (i) heat flux through the sea surface, (ii) heat flux through the base of the mixed layer by mixing and upwelling/downwelling and (iii) horizontal advection.

Let us first consider tropical latitudes. Fig.11.8 illustrates important aspects of the air-sea flux contribution there. We take a mean air temperature $T_{air} = 27^\circ\text{C}$ which yields a specific humidity of about 15 g kg^{-1} if the relative humidity is 70%. Assuming a mean wind-speed of 3 m s^{-1} , the contributions of the Q_{SW} , Q_{LW} , Q_S and Q_L are plotted as functions of SST using bulk

²At low temperatures typical of polar oceans, α_T varies strongly with T and p and becomes smaller at lower temperatures and increases with depth, especially in the Weddell and Greenland Seas — see Table 9.4. The excess acceleration of a parcel resulting from the increase of α_T with depth (known as the thermobaric effect), can result in a destabilization of the water column if the displacement of a fluid parcel (as a result of gravity waves, turbulence, or convection) is sufficiently large.

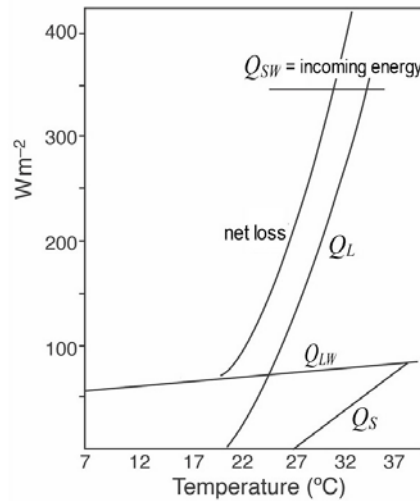


Figure 11.8: Contributions of the air-sea flux terms: Q_{SW} , the incoming solar radiation and Q_{LW} , Q_S and Q_L making up the net loss term (see Eq.11.5) plotted as a function of SST using bulk formulae, Eqs.(11.6) and (11.7).

formulae, Eqs.(11.6) and (11.7). The shortwave incoming radiation reaching the surface is assumed to be 341W m^{-2} and is offset by back radiation Q_{LW} , sensible heat loss Q_S (when SST> 27°C) and evaporative loss Q_L . Because Q_L rises very steeply with temperature there is a natural limit on the tropical SST that depends on the radiation available and the wind-speed. For the parameters chosen, energy supply and loss balance at an SST of about 30°C : at temperatures only slightly above this limit, evaporative losses far exceed the possible input of radiation, limiting SST. This evaporative feedback explains why tropical temperatures are so stable. In fact some energy is carried down into the interior ocean and the solar energy is absorbed in the top few meters rather than right at the surface. Nevertheless, the limit on SST due to surface processes illustrated in Fig.11.8 is very much at work in regulating surface temperatures in the tropics.

In the subtropics, evaporation is the principal heat loss term (see Fig.11.3) and varies comparatively little throughout the year. Due to the seasonal cycle of insolation, there is a net deficit of energy in the winter and a net excess in the summer. Along with cooling to the atmosphere, upwelling of deep cold fluid in the subpolar gyres helps to maintain low surface temperatures

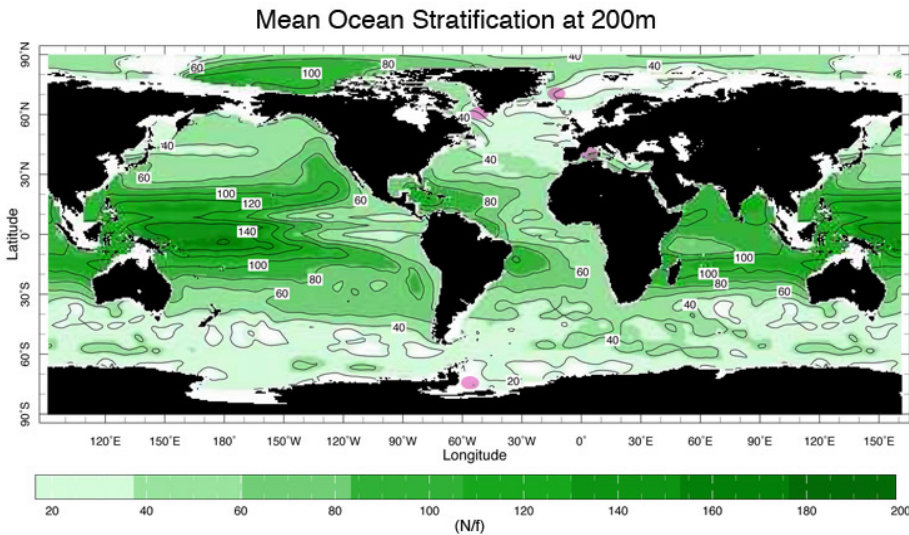


Figure 11.9: The annual mean stratification of the ocean at a depth of 200 m, as measured by $\frac{N}{f_{ref}}$: i.e. the buoyancy frequency, Eq.(9.6), normalized by a reference value of the Coriolis parameter, $f_{ref}=10^{-4} \text{ s}^{-1}$. Note that $\frac{N}{f_{ref}} \lesssim 20$ in regions where deep mixed layers are common — cf. Fig.9.10. Sites of deep-reaching convection are marked in the Labrador Sea, the Greenland Sea, the Western Mediterranean and the Weddell Sea.

in polar latitudes. At very high latitudes there is a net buoyancy loss out of the ocean in regions of very weak stratification. This, as discussed below, can trigger deep-reaching convection creating very deep mixed layers that can ventilate the abyss.

Small-scale turbulent mixing in the ocean allows temperature changes at the surface to be communicated to deeper layers, as sketched in Fig.9.11. Wind-generated turbulence often creates almost isothermal conditions in the top 20 – 50 m of the ocean with a sharp discontinuity at the base. Another major factor in determining the distribution of surface properties is the pattern of Ekman pumping shown in Fig.10.11. For example, in the equatorial belt the trade winds drive Ekman transport away from the equator drawing cold water up from below: the surface temperature can be actually lower directly along the equator than immediately to the north or south!

Such considerations of energy balance at the surface and wind-induced



Figure 11.10: The Woods Hole ship KNORR cuts through harsh Labrador Sea conditions during the winter Labrador Sea Deep Convection Experiment (Feb–Mar 1997) taking observations shown in Fig.11.11. Waves such as those shown at the top caused continual ice build-up on the ship, as can be seen at the bottom. Courtesy of Bob Pickart, WHOI.

Ekman pumping and turbulence, provide a first-order explanation of many of the major features of the SST distribution and its seasonal variation shown in Fig.9.3, and reflect variations in the available solar radiation modified by air-sea fluxes of sensible and latent heat, advection (both horizontal and vertical) and mixing of properties with deeper layers. These processes are frequently interpreted in terms of vertical one-dimensional models which attempt to represent the turbulent transfer of heat and buoyancy through the mixed layer, by wind and convectively driven turbulence, and its communication with the ocean below through entrainment and vertical motion.

It is also worthy of note that the North Atlantic is warmer than both the North Pacific and the Southern Ocean at the same latitude in the same season. The warmth of the Atlantic relative to the Pacific is thought to be largely a consequence of differences in the surface wind patterns. In the North Atlantic the zero wind-stress curl line (along which the interior extension of the western boundary currents tends to flow) slants much more than in the Pacific, allowing the Gulf Stream to carry warm surface waters into far northern latitudes in the Atlantic.

11.1.3 Sites of deep convection

A comparison of Figs.11.4 and 11.6 with Fig.9.10 shows that there is no direct relationship between the pattern of air-sea buoyancy forcing and the pattern of mixed layer depth. This is because the strength of the underlying stratification plays an important role in ‘preconditioning’ the ocean for convection. The deepest mixed layers are seen in the polar regions of the winter hemisphere and are particularly deep in the Labrador and Greenland Seas of the North Atlantic, where they can often reach depths well in excess of 1 km. Here the ambient stratification of the ocean is sufficiently weak and the forcing sufficiently strong to trigger deep-reaching convection and bring fluid from great depth into contact with the surface. Note that deep mixed layers are notably absent in the North Pacific ocean. Waters at the surface of the north Pacific are relatively fresh (note, for example, how much fresher is the surface Pacific than the Atlantic in Fig.9.4) and remain buoyant even when cooled. Deep mixed layers over wide areas of the southern oceans in winter are also observed, but they are considerably shallower than their counterparts in the northern North Atlantic.

Evidence from observations of mixed layer depth and interior tracer distributions reviewed below in Section 11.2.1, suggest that convection reaches

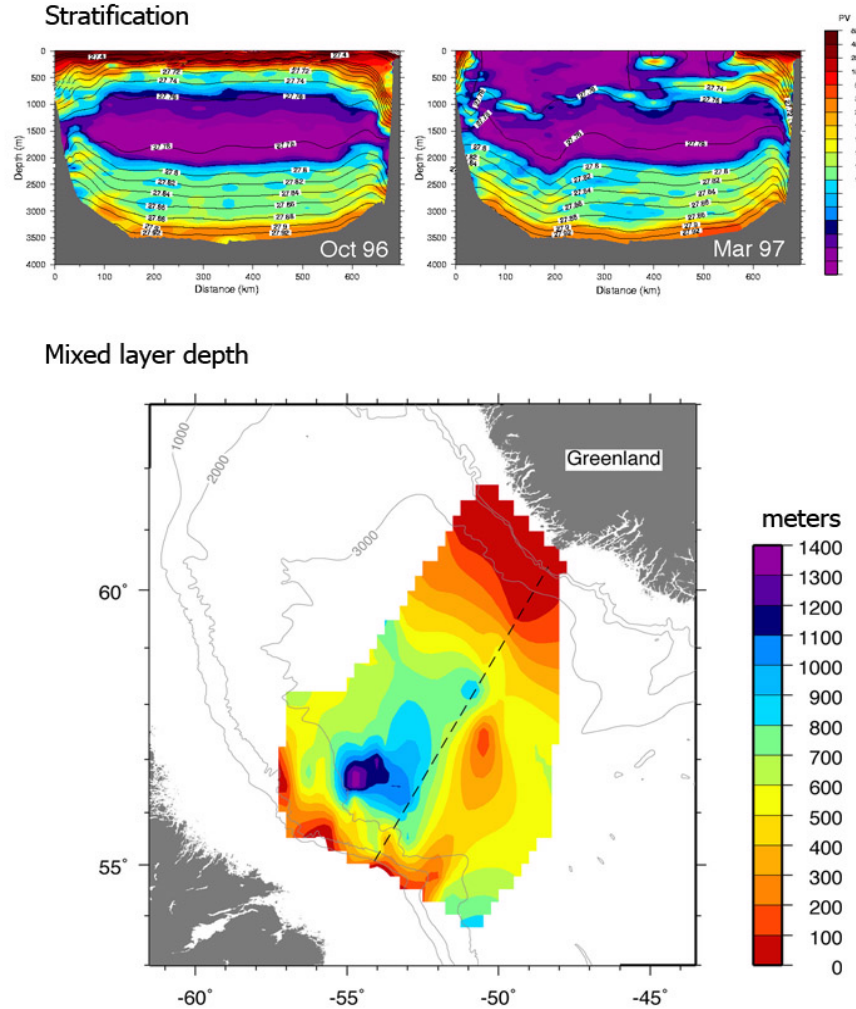


Figure 11.11: Top: Sections of potential density, σ (contoured) and stratification, $\frac{\partial \sigma}{\partial z}$ (colored) across the Labrador Sea in October 1996, prior to the onset of convection and in March 1997, after, and during wintertime convection. Purple indicates regions of very weak stratification. Bottom: A horizontal map of mixed layer depth observed in Feb-Mar 1997, showing convection reaching to depths in excess of 1 km. The position of the sections shown at the top is marked by the dotted line. Courtesy of Robert Pickart, WHOI.

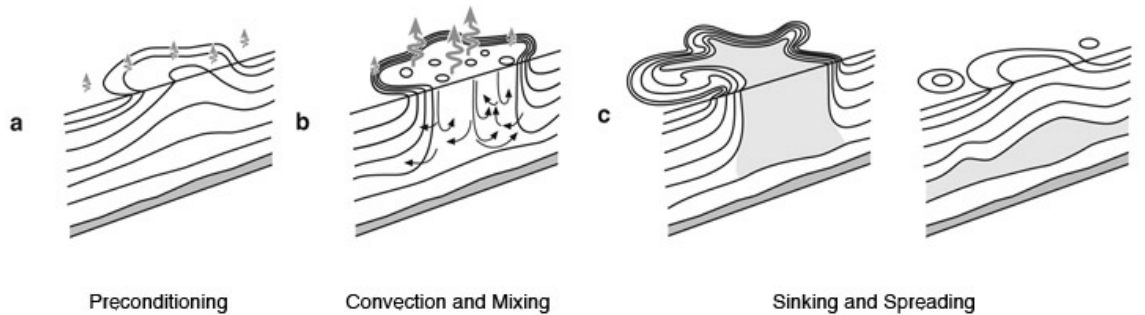


Figure 11.12: Schematic diagram of the three phases of open-ocean deep convection: (a) preconditioning, (b) deep convection and mixing and (c) sinking and spreading. Buoyancy flux through the sea surface is represented by curly arrows, and the underlying stratification/outcrops are shown by continuous lines. The volume of fluid mixed by convection is shaded. From Marshall and Schott (1999).

down into the abyssal ocean only in the Atlantic (in the Labrador and Greenland Seas) and also in the Weddell Sea, as marked in Fig.11.9. These sites, despite their small areal extent, have global significance in setting and maintaining the properties of the abyss. They are thought to play a major role in climate variability (see Chapter 12.3.5). Observations suggest that there are certain common features and conditions that predispose these regions to deep-reaching convection. First, there is strong atmospheric forcing because of thermal and/or haline surface fluxes (see Fig.11.4). Thus open ocean regions adjacent to boundaries are favored, where cold, dry winds from land or ice surfaces blow over water inducing large sensible and latent heat and moisture fluxes. Second, the stratification beneath the surface-mixed layer is weak, made weak perhaps by previous convection. And third, the weakly stratified underlying waters are brought up toward the surface so that they can be readily and directly exposed to buoyancy loss from the surface. This latter condition is favored by cyclonic circulation associated with density surfaces, which ‘dome-up’ to the surface, drawn upward by Ekman suction over subpolar gyres (Fig.10.11). In places where deep convection is occurring, weak vertical buoyancy gradients are observed (see Fig.11.9, which plots N , Eq.(9.6), at a depth of 200 m over the global ocean) and isopycnals dome up toward the surface (see Fig.9.7).

Observations of deep convection

Observations at sea during deep convection are rare because of the inhospitable conditions in which wintertime convection occurs: see the photographs taken from a research vessel in the Labrador Sea in winter presented in Fig.11.10. The best-observed region of deep convection is the Labrador Sea. Fig.11.11 shows sections of σ and N through the Labrador Sea just prior to (fall 1996) and during/after wintertime deep convection. In October we see a near-surface stratified layer, some 500 m or so in depth, overlaying a relatively well-mixed intermediate layer, formed by prior convection. By March of the following year, however, convection triggered by cooling from the surface has broken through the stratified layer, mixing intermediate and surface fluid and leading to a well mixed patch of some 200 km in horizontal extent by, in places, 1500 m in depth. Just as in our studies of convection in water heated from below described in Section 4.2.4, cooling of the ocean from above results in convection which returns the fluid to a state of neutral stability with a well-mixed column in which $N \rightarrow 0$. By the following fall (not shown but similar to the October section of Fig.11.11) the mixed patch has been ‘covered up’ by stratified fluid sliding over from the side. The water mass formed by convection in the previous winter, now exists as a subsurface bolus of fluid which in the subsequent months and years is drawn into the interior of the ocean. The process has been likened to a chimney, but is perhaps better described as analogous to the way in which a snake swallows an egg, as sketched in the schematic diagram setting out the phases of deep convection in the ocean shown in Fig.11.12.

11.2 The observed thermohaline circulation

The time-mean abyssal flow in the ocean is so weak that it cannot be measured directly. However abyssal circulation, and the convective processes forcing it, leaves its signature in the distribution of water properties, from which much can be inferred.

11.2.1 Inferences from interior tracer distributions

Water masses modified by deep convection are tagged with T and S values characteristic of their formation region (together with other tracers such as tritium from the atomic weapon tests of the 1960’s and chlorofluorocarbons

(CFC's) from industrial and household use. Tracers to be tracked far from their formation region, revealing interior pathways through the ocean.

Zonal-average sections of T and S across the Atlantic Ocean are shown in Fig.11.13: see also the hydrographic section along 25°W in the Atlantic shown in Fig.9.9. We see three distinct layers of deep and abyssal ocean water, fed from different sources. Sliding down from the surface in the southern ocean to depths of 1 km is ‘Antarctic Intermediate Water’ (AAIW), with low salinity (34.4psu) and, near the surface, slightly lower temperature than water immediately above and below. This water appears to originate from about 55°S and is associated with regions of deep mixed layers in the circumpolar ocean seen in Fig.9.10. At a depth of 2 km or so — indeed, filling most of the Atlantic basin — is ‘North Atlantic Deep Water’ (NADW), with high salinity (34.9psu) originating in high northern latitudes, but identifiable as far south as 40°S and beyond. At the very bottom of the ocean is ‘Antarctic Bottom Water’ (AABW), less saline but colder (and denser) than NADW. Together, these give us a picture of a multilayered pattern of localized sinking and horizontal spreading of the dense water, which were represented schematically by the arrows in Fig.11.1.

Another useful tracer of the circulation is dissolved oxygen. Surface waters are near saturation in oxygen content (in fact, they are slightly super-saturated). As the water leaves the surface (the source of oxygen), its oxygen content is slowly used up by biological activity. Hence, oxygen content gives us a sort of clock by which we can get a feel for the “age” of the water (*i.e.*, the time since it left the surface); the lower the content, the ‘older’ the water. Oxygen content (expressed as a percentage of saturation) for the Atlantic and Pacific Oceans is shown in Figs.11.14, top and bottom, respectively.

In the Atlantic, water in the deep ocean shows a progressive aging from north to south, implying the dominant source is in the far north. However, the water is generally ‘young’ (oxygen saturation > 60%) everywhere except at depths shallower than 1 km in low latitudes, where ‘old’ water is (we infer) slowly upwelling from below (cf. the isopycnals in Fig.9.7). That water is relatively young near the Antarctic coast, around 40° – 50°S and, especially, in high northern latitudes, is evidence that surface waters are being mixed down in these regions of the Atlantic. In contrast, the Pacific Ocean cross-section, Fig.11.14(bottom), shows young water only near the Antarctic: deep water in high northern latitudes has very low oxygen content, from which we infer that there is no sinking of surface waters in the north Pacific, except in the Arctic basin.

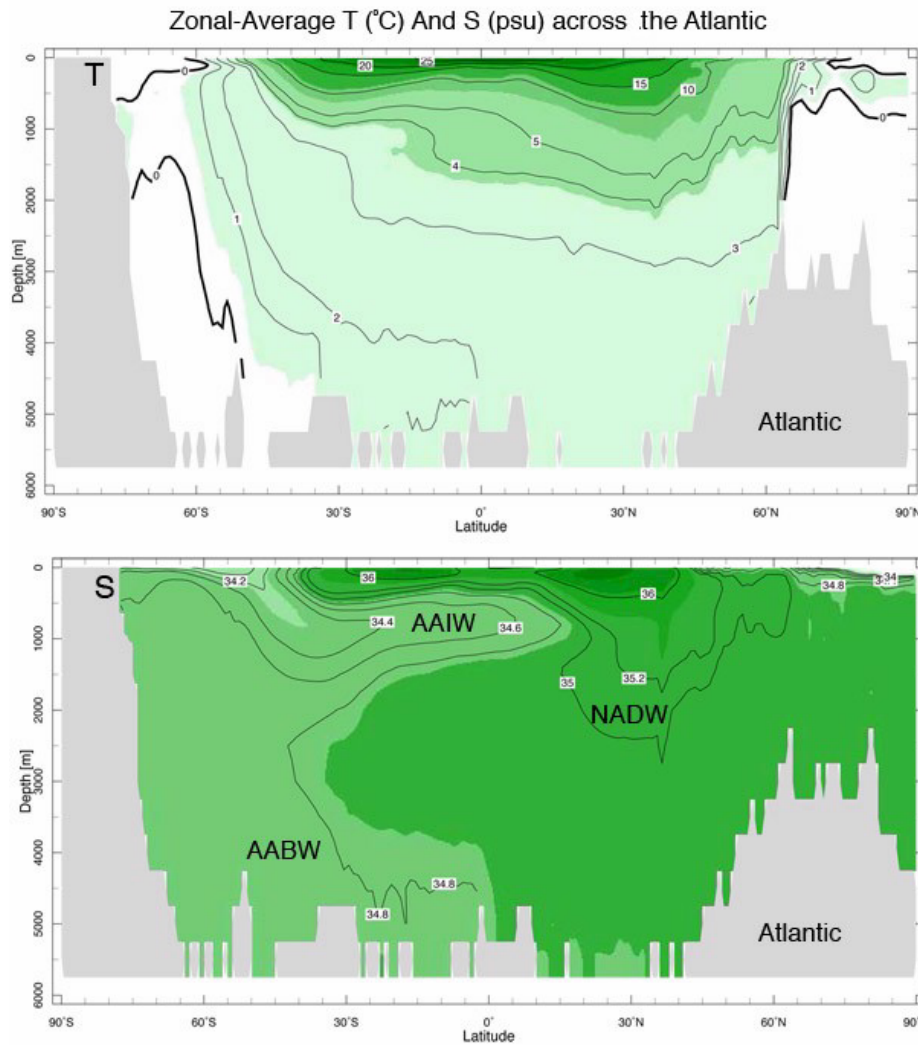


Figure 11.13: Zonal average ($0^{\circ} \rightarrow 60^{\circ}$ W) temperature (top) and salinity (bottom) distributions across the Atlantic Ocean. Antarctic Intermediate Water (AAIW), Antarctic Bottom Water (AABW) and North Atlantic Deep Water (NADW) is marked. Compare this zonal-average section with the hydrographic section along 25° W shown in Fig.9.9.

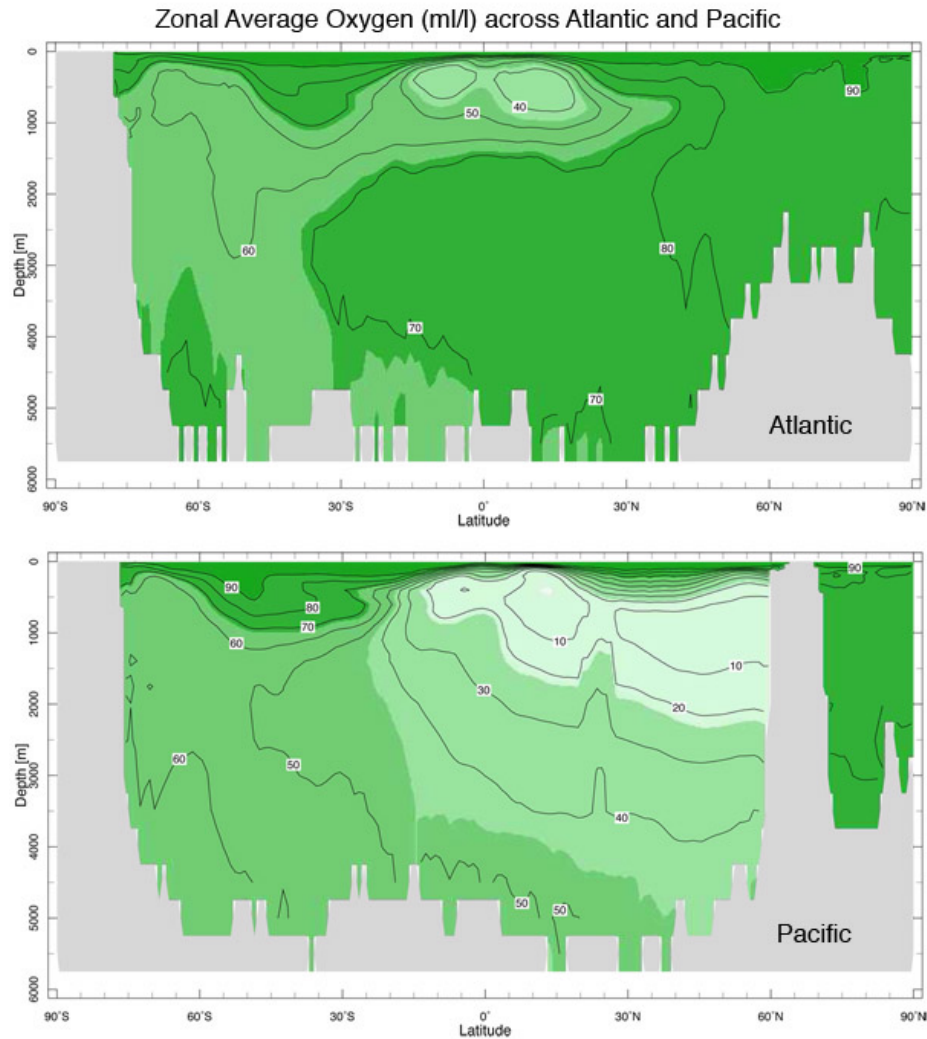


Figure 11.14: Zonally averaged oxygen saturation (in ml l^{-1}) in the Atlantic (0° – 60°W) and Pacific (150° – 190°W) oceans.

11.2.2 Time scales and intensity of thermohaline circulation

Water whose properties are set (oceanographers use the term ‘formed’) at the source regions marked in Fig.11.9 must spread out before slowly upwelling back to the surface to complete the circuit of mass flow. Estimates of the strength of the major source, NADW, are about 14Sv (see Section 11.4). Using this source rate we can make several estimates of parameters indicative of the strength of the circulation. The area of the Atlantic Ocean is about 10^{14} m^2 . The depth of the ocean ventilated by the surface sources is perhaps 3 km (see Fig.11.13). So one estimate of the time scale of the overturning circulation is $\tau = \frac{\text{ocean volume}}{\text{volume flux}} = \frac{10^{14} \text{ m}^2 \times 3 \times 10^3 \text{ m}}{1.4 \times 10^7 \text{ m}^3 \text{ s}^{-1}} \simeq 700 \text{ y}$. The net horizontal flow velocity in the deep ocean must be about $v = \frac{\text{volume flux}}{\text{depth} \times \text{width}} = \frac{1.4 \times 10^7 \text{ m}^3 \text{ s}^{-1}}{3 \times 10^3 \text{ m} \times 5 \times 10^6 \text{ m}} \simeq 10^{-3} \text{ m s}^{-1}$. If compensating upwelling occupies almost all of the ocean basin, the upwelling velocity must be about $w = \frac{\text{volume flux}}{\text{area of ocean}} = \frac{1.4 \times 10^7 \text{ m}^3 \text{ s}^{-1}}{10^{14} \text{ m}^2} \simeq 4 \text{ m y}^{-1} (!!)$, ten times smaller than typical Ekman pumping rates driven by the wind (cf. Fig.10.11).

Thus, the interior abyssal circulation is very, very weak, so weak that it is all but impossible to observe directly. Indeed progress in deducing the likely pattern of large-scale abyssal circulation has stemmed as much from the application of theory as direct observation, as we now go on to discuss.

11.3 Dynamical models of the thermohaline circulation

11.3.1 Abyssal circulation schematic deduced from ‘Taylor-Proudman’ on the sphere

Because of the paucity of direct observations of abyssal flow, theory has been an invaluable guide in deducing likely circulation patterns. The starting point for a theoretical deduction are two important inferences from the observations discussed above:

1. dense water is formed at the surface in small, highly localized regions of the ocean in polar seas. Thus the abyssal circulation seems to be induced by *local* sources, marked in Fig.11.9. But for every particle of water that sinks, one must return to the surface. Property distributions

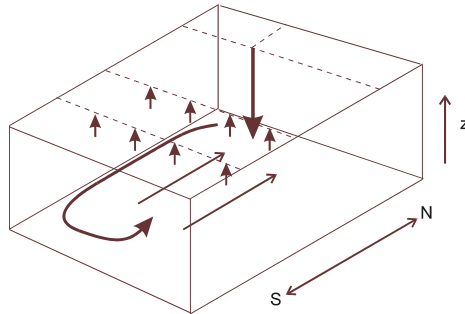


Figure 11.15: Water is imagined to sink in a localized region in polar latitudes (the single long arrow pointing downward) with compensating upwelling distributed over the basin (the many short arrows pointing upward). Taylor columns in the interior are therefore stretched and move toward the pole satisfying Eq.(11.8). The poleward motion over the interior is balanced by equatorward flow in a western boundary current.

reviewed in Section 11.2.1 suggest that the return branch does not occur in one, or a few, geographical locations. It seems reasonable to suppose, therefore, that there is widespread compensating upwelling on the scale of the basin, as sketched in our schematic diagram used to introduce this chapter, Fig.11.1.

2. the deep flow is sluggish with very long timescales. It will therefore be in geostrophic, hydrostatic and thermal wind balance. Moreover Eq.(10.12) will be appropriate, telling us that if columns of fluid are stretched or squashed then meridional motion results.

In the region of upwelling (which, we can surmise, is almost all the ocean) fluid columns in the homogeneous abyss must behave like Taylor columns and the geostrophic flow on the planetary scale will be divergent. Thus integrating Eq.(10.12) from the bottom up to mid-depth in the water column, we find:

$$\int_{\text{bottom}}^{\text{mid-depth}} v dz = \frac{f}{\beta} w_{\text{mid-depth}} > 0 \quad (11.8)$$

where we have set $w_{bottom} = 0$ (assuming a flat bottom) and supposed $w_{mid-depth} > 0$, directed upwards, as sketched in Fig.11.1 and 11.15. Thus fluid columns must move poleward, *towards* the deep water mass source!

We can interpret this result in terms of our discussion of T-P on the sphere in Chapter 10. There we found that Taylor columns in the thermocline of the subtropical gyres move equatorward in order to accommodate Ekman pumping driven from above by the curl of the wind stress. In the present context we deduce that abyssal columns in the interior of the ocean must move *poleward* in response to upwelling at mid-depth, compensating for polar sinking. Referring back to Fig.10.15b and simply reversing the sign of the arrows, we see that by moving poleward, Taylor columns will stretch in a direction parallel to Ω relative to the spherical, horizontal, surfaces, producing the required upwelling.

How can the interior poleward circulation be closed? The answer is that, once again, we have to rely on western boundary currents to close the circuit, as sketched in Fig.11.15 and discussed in Section 11.3.3. Thus, for example, the poleward interior flow in the north Atlantic is returned to the south, along with source waters, in a *western* boundary current. Such considerations led Henry Stommel³ to his classic schematic of deep thermohaline circulation shown in Fig.11.16 driven by sinking in the northern North Atlantic and the Weddell Sea in Antarctica. Note that the interior flow is directed poleward everywhere in accord with Eq.(11.8). Fluid from the sinking regions is carried away in western boundary currents. Thus Stommel hypothesized the existence of a boundary current in the North Atlantic flowing southward at



³ Henry Melson Stommel, 1920-1992, was the most influential dynamical oceanographer of all time. A theorist who made observations at sea and also worked in the laboratory, Stommel shaped the field and contributed many of the seminal ideas that led to the development of our understanding of the wind-driven (Chapter 10) and thermohaline circulation of the ocean (Chapter 11). Stommel joined the Woods Hole Oceanographic Institution (WHOI) in 1944 and left in 1959 to become a professor first briefly at Harvard, then at MIT before returning to WHOI (his spiritual home) in 1979.

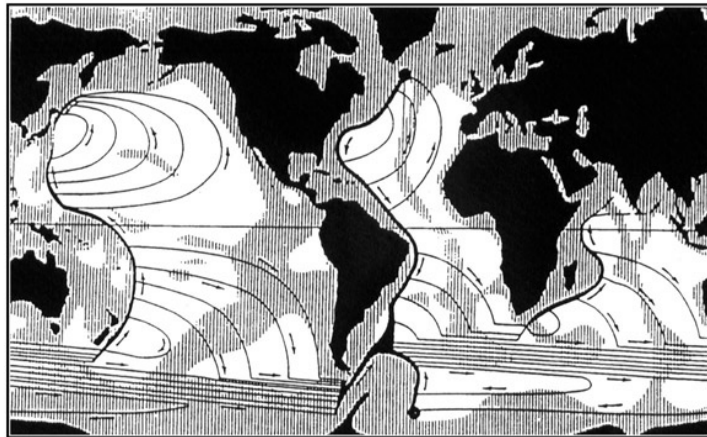


Figure 11.16: Schematic of the abyssal circulation in the ocean deduced by Stommel (1958) based on consideration of Eq.(10.12) and its vertical integral, Eq.(11.8). He imagined that the abyssal ocean was driven by sinking in two regions, the Labrador-Greenland Sea and the Weddell Sea, represented by the large black dots. Upwelling over the interior of the ocean led to interior poleward motion with return flows in western boundary currents. The shaded areas represent regions of elevated topography — c.f. Fig.9.1.

depth, beneath the Gulf Stream! As we shall discuss in Section 11.4, this was subsequently confirmed by direct observation.

11.3.2 GFD Lab XIV: The abyssal circulation

A laboratory experiment can be used to vividly illustrate the dynamical ideas that underpin the abyssal circulation schematic, Fig.11.16, proposed by Stommel. It was first carried out in Woods Hole by Stommel and collaborators. The apparatus is shown in Fig.11.17 and described in the legend. We use the same tank as in the ‘wind-driven circulation’ experiment (GFD Lab XIII, described in Section 10.2.4) with a sloping base to represent spherical effects, but without the rotating disc above. Dyed water is introduced very slowly, through a ‘diffuser’ in the shallow end of the tank (representing polar latitudes). The surface of the water thus rises, stretching interior Tay-

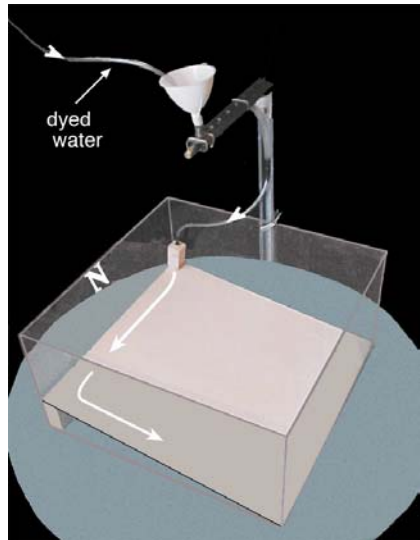


Figure 11.17: Apparatus used to illustrate the driving of deep ocean circulation by localized sinking of fluid. A sloping base is used to represent the influence of sphericity on Taylor columns as in GFD XIII. The 50 cm square tank is filled with water and set rotating anticlockwise at a rate of $\Omega = 5\text{ rpm}$. (The sense of rotation is thus representative if the northern hemisphere). Dyed water, supplied via a funnel from an overhead bucket, flows slowly in to the tank through a diffuser located in the ‘north east’ corner at a rate of typically $20 \text{ cm}^3 \text{ min}^{-1}$ or so. The circulation of the dyed fluid is viewed from above using a camera.

lor columns which therefore move toward the shallow (poleward) end of the tank. Boundary currents develop on the poleward and western boundaries supplying fluid to the deep end (equatorward) of the tank, just as sketched in Fig.11.15.

Development of the flow and the existence of boundary currents can be clearly seen by charting the evolution of the dye, as shown in Fig.11.18. Rather than moving away in to the interior directly from the source, we observe westward flow along the northern boundary and then southward flow in a western boundary current. The tank thus fills up via boundary currents which ultimately ‘supply’ the interior. Note also how turbulent the flow patterns are — even in this controlled laboratory experiment, in which fluid was introduced very slowly, we do not observe steady, laminar flow.

Rather, there is much time-dependence and recirculation of fluid between the interior and the boundary currents, a feature of deep boundary currents in the real ocean.

Application of T-P theory to the experiment

We now apply dynamical ideas to the experiment in a way that directly parallels that developed in Section 11.3.1 to infer abyssal circulation patterns in the ocean. If fluid is introduced to the tank of side L at rate \mathcal{S} , then the depth of the fluid in the tank, h , — see Fig.11.19 — increases at a rate given by:

$$\frac{dh}{dt} = \frac{\mathcal{S}}{L^2}$$

In the presence of rotation, columns of fluid in steady, slow, frictionless motion must, by the Taylor-Proudman theorem, remain of constant length. Hence, if the free surface rises, an interior column, marked by the thick vertical line in Fig.11.19, must move toward the shallow end of the tank *conserving its length*. In a time Δt the free surface has risen by Δh and so the vertical velocity is $w = \frac{\Delta h}{\Delta t} = \frac{\mathcal{S}}{L^2}$, from above. Given that the displacement of the column must match the geometry of the wedge defined by the upper surface and the sloping bottom, we see that the vertical and horizontal velocity must be in the ratio $\frac{w}{v} = \frac{dz}{dy} = \alpha$, where α is the slope of the bottom and we have used the definitions $w = \frac{dz}{dt}$, $v = \frac{dy}{dt}$. Thus v is given by:

$$v = \frac{w}{\alpha} = \frac{1}{\alpha} \frac{\mathcal{S}}{L^2} \quad (11.9)$$

exactly analogous to Eq.(11.8).⁴ The column moves northwards, towards the shallow end of the tank i.e. ‘polewards’.

Typically we set $\mathcal{S} = 20 \text{ cm}^3 \text{ min}^{-1}$, $\alpha = 0.2$, $L = 50 \text{ cm}$, and so we find that $v = \frac{1}{0.2} \times \frac{20 \text{ cm}^3 \text{ min}^{-1}}{50 \text{ cm}^2} = 3.3 \times 10^{-4} \text{ m s}^{-1}$, or only 20 cm in 10 min. The boundary currents returning the water to the deep end of the tank are much swifter than this and are clearly evident in Fig.11.18.

⁴Comparing Eqs.(11.9) and (11.8), we see that α plays the role of $\frac{\beta D}{f} \sim \frac{D}{a}$ (since, see Eq.(10.10), $\beta \sim \frac{f}{a}$) where D is a typical ocean depth and a is the radius of the earth. It is interesting to note that Ω does not appear in either Eq.(11.9) or (11.8) — nevertheless it is important to realise that rotation is a crucial ingredient through imposition of the T-P constraint.

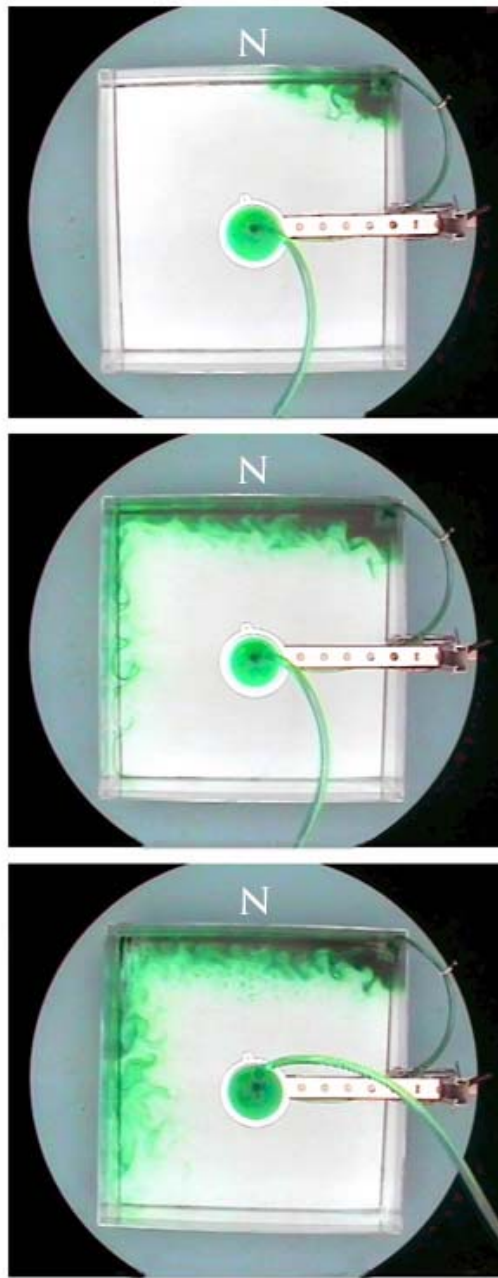


Figure 11.18: Three photographs, at 10 min intervals, charting the evolution of dye slowly entering a rotating tank of water with a sloping bottom, as sketched in Fig.11.17. The funnel in the centre carries fluid to the diffuser located at the top right hand corner of the tank. The shallow end of the tank is marked with the ‘N’ and represents polar latitudes. The dyed fluid enters at the top right, and creates a ‘northern’ and then ‘western’ boundary current.

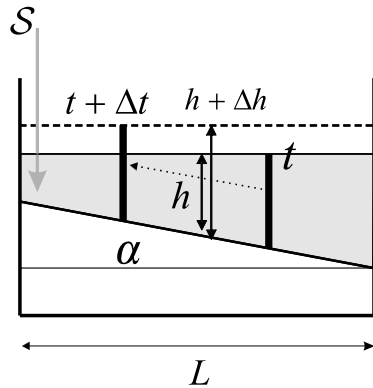


Figure 11.19: Fluid entering the tank at rate S leads to a rise in the free surface, h . The Taylor Column marked by the vertical thick line therefore moves toward the shallow end of the tank (dotted arrow), conserving its length. The bottom tilts at an angle α .

Our experiment confirms the preference for *western* boundary currents. But why are western boundary currents favored over eastern boundary currents? In Chapter 10 we explained the preference of wind-driven ocean gyres for western, as opposed to eastern boundary currents, by invoking an interior Sverdrup balance, Eq.(10.17), and arguing that the sense of the circulation must reflect that implied by the driving wind. But in the present context there is no wind-stress to dictate the sense of the circulation. What's going on?

11.3.3 Why western boundary currents?

Let's first review what we can deduce by application of the Taylor-Proudman theorem alone. Taylor-Proudman says (see Section 7.2) that, *if the motion of a rotating, homogeneous fluid is sufficiently slow, steady and frictionless*, then columns parallel to the rotation vector will not tip over or change their length. Thus if T-P is obeyed, the length of a column is conserved as it moves.

The conditions in italics above are most likely to be satisfied in the interior of our rotating tank where, in the presence of a rising free surface, interior columns conserve their length by moving poleward — see Fig.11.19. They are most likely to be violated at the lateral walls where frictional effects begin

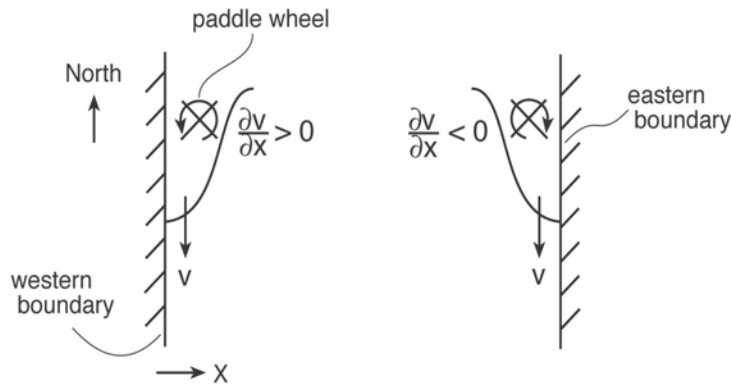


Figure 11.20: Schematic diagram of boundary currents in the laboratory experiment shown in Fig.11.18 and Fig.11.22. The mass balance of Taylor columns moving in boundary currents on the western margin (whether southwards as sketched here or northward) can be satisfied; the mass balance of Taylor columns moving in boundary currents on the eastern margin (whether running north or south) cannot.

to play a role allowing, as we shall see, fluid columns to change their length by either shedding or accumulating mass. On consideration of further factors (see below), it turns out that western boundary currents are favored. A jet just cannot make it far if it slides along an eastern boundary, as we now go on to discuss.

Consider the geostrophic relation with f constant, but now let's incorporate a simple representation of frictional drag, as in Eq.(7.28) where we discussed atmospheric winds in the Ekman layer. The modified geostrophic balance, Eq.(7.25), then becomes, written out for convenience here in component form:

where k is a drag coefficient representing the rubbing of the Taylor column over the bottom and δ is the Ekman layer depth. Now, just as in the derivation of the T-P theorem in Section 7.2, we cross-differentiate the above to eliminate the pressure p , to obtain:

$$f \left(\frac{\partial u}{\partial x} + \frac{\partial v}{\partial y} \right) = -\varepsilon \left(\frac{\partial v}{\partial x} - \frac{\partial u}{\partial y} \right).$$

where for convenience we have introduced $\varepsilon = \frac{k}{\delta}$. Now, since, by continuity, $\left(\frac{\partial u}{\partial x} + \frac{\partial v}{\partial y} \right) = -\frac{\partial w}{\partial z}$, the above can be written:

$$f \frac{\partial w}{\partial z} = \varepsilon \left(\frac{\partial v}{\partial x} - \frac{\partial u}{\partial y} \right) \quad (11.10)$$

What is Eq.(11.10) saying physically? If the flow is frictionless ($\varepsilon = 0$), the rhs is zero and we recover a version of Eq.(7.15), the T-P theorem;

$$f \frac{\partial w}{\partial z} = 0$$

But the theorem is violated by the presence of friction which allows columns to stretch or squash at a rate that depends on ε and $\frac{\partial v}{\partial x} - \frac{\partial u}{\partial y}$.

The quantity $\zeta = \left(\frac{\partial v}{\partial x} - \frac{\partial u}{\partial y} \right)$ is the vertical component of a vector called the vorticity, which measures the spin of a fluid parcel about a vertical axis relative to the rotating earth (or table). Imagine that we place a miniature, weightless paddle wheel in to a flow which floats along with a fluid parcel and spins around on its vertical axis. It turns out that the vorticity ζ is exactly twice the rate of rotation of the paddle wheel (see Q7, Chapter 6). For example, a paddle wheel placed in a swirling flow such as that sketched in Fig.7.26(left) will spin cyclonically, $\left(\frac{\partial v}{\partial x} - \frac{\partial u}{\partial y} \right) > 0$. Thus Eq.(11.10) then implies $\frac{\partial w}{\partial z} > 0$: so, since $w = 0$ at the bottom, fluid will upwell away from the boundary and the column will stretch. Cross-isobaric flow at the bottom fluid, where the column rubs over the base of the tank, leads to the requisite acquisition of mass. This is exactly the same process studied in GFD Lab X: fluid is driven in to a low pressure system at its base where frictional affects are operative — see Fig.7.23(top).

Now let us return to the problem of boundary currents. Consider the southward flowing western boundary current sketched in Fig.11.20. A paddle wheel placed in it will turn cyclonically because flow on its inside flank is faster than on its outside flank. Hence $\left(\frac{\partial v}{\partial x} - \frac{\partial u}{\partial y} \right) > 0^5$. Now using Eq.(11.10) we see that $\frac{\partial w}{\partial z} > 0$. But this is just what is required of a southward flowing boundary current (moving to the deeper end of the tank) because, from Eq.(11.10), it must stretch, $\frac{\partial w}{\partial z} > 0$. Thus the signs in Eq.(11.10) are consistent. But what happens in the southward flowing eastern boundary current sketched on the right of Fig.11.20? There $\left(\frac{\partial v}{\partial x} - \frac{\partial u}{\partial y} \right) < 0$ and so Eq.(11.10)

⁵This is obvious since, by definition, $|v| >> |u|$ and $\frac{\partial}{\partial x} >> \frac{\partial}{\partial y}$ in a meridional boundary current.

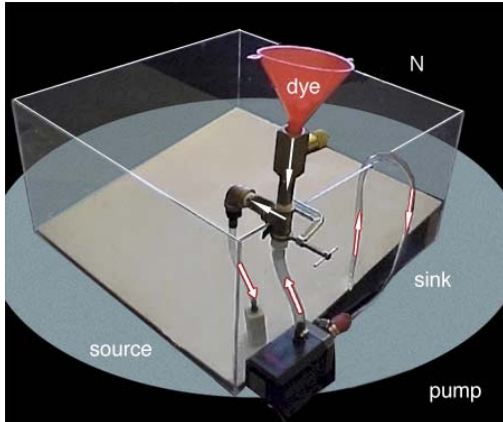


Figure 11.21: Source-sink driven flow can be studied with the apparatus shown above. The pump and associated tubing can be seen, together with the intravenous device used to dye the fluid travelling toward the source. Fluid enters the tank through a submerged diffuser. The pumping rate is very slow — only about $20 \text{ cm}^3 \text{ min}^{-1}$. An example of the subsequent evolution of the dyed fluid is shown in Fig.11.22.

tells us that $\frac{\partial w}{\partial z} < 0$. But this is the wrong sign if the column is to stretch. Thus we conclude that the southward flowing eastern boundary current cannot satisfy Eq.(11.10) and so is disallowed. On consideration of the balance of terms in northward flowing boundary currents, we deduce that eastern boundary currents of both signs are prohibited, but western boundary currents of both signs are allowed.

11.3.4 GFD Lab XV: Source sink flow in a rotating basin

The preference for western, as opposed to eastern, boundary currents can be studied in our rotating tank by setting up a source/sink flow using a pump, as sketched in Fig.11.21. The pump gently draws fluid out of the tank (to create a sink) and pumps it back in through a diffuser (the source). On the way the fluid is dyed (through an intravenous device) so that when it enters at the source its subsequent path can be followed. Experiments with different arrangements of source and sink are readily carried out. [See Problem 3 at

end of the Chapter]. One example is shown in Fig.11.22. Fluid is sucked out toward the northern end of the eastern boundary (marked by the black circle) and pumped in on the southern end of the eastern boundary (marked by the white circle). Rather than flow due north along the eastern boundary, fluid tracks west, runs north along the western boundary and then turns eastwards at the ‘latitude’ of the sink. And all because eastern boundary currents are disallowed!

11.4 Observations of abyssal ocean circulation

It is very hard to test whether the circulation schematic, Fig.11.16, has parallels in the ocean because the predicted mean currents are so very weak and the variability of the ocean so strong. However, one of the key predictions of Stommel’s abyssal theory was that there ought to be deep western boundary currents which are sufficiently strong that they can be directly observed. In a rare case of theory preceding observation, the Deep Western Boundary Current on the Atlantic continental rise south of Cape Cod was indeed subsequently confirmed by direct observation.

There is also definitive evidence of deep western boundary currents in hydrographic sections. For example, Fig.11.23 — a cross-section of water properties at 30°S — shows NADW, formed by convective processes in the northern North Atlantic, flowing as a deep, relatively salty, western boundary current in to the South Atlantic. One can also detect Antarctic Bottom Water, flowing northward as a relatively fresh, but very cold body of water, right at the bottom. The entire abyssal ocean is supplied via these western boundary currents, which feed the interior circulation of the open ocean. Other regions of the world ocean are also fed from the Atlantic, but by a more circuitous route which involves the Antarctic Circumpolar Current, as roughly captured by Stommel’s remarkable schematic.

One very vivid depiction of the abyssal circulation is revealed by the pathways of CFC from the ocean surface in to the interior shown in Fig.11.24. Recall, CFC’s (see Table 1.2) are man-made substances and only appeared in the 20th Century. The atmospheric concentration of CFC-11 increased dramatically in the middle part of the last century and dissolved in to surface waters. They were first observed invading the ocean in the 1960’s. At high

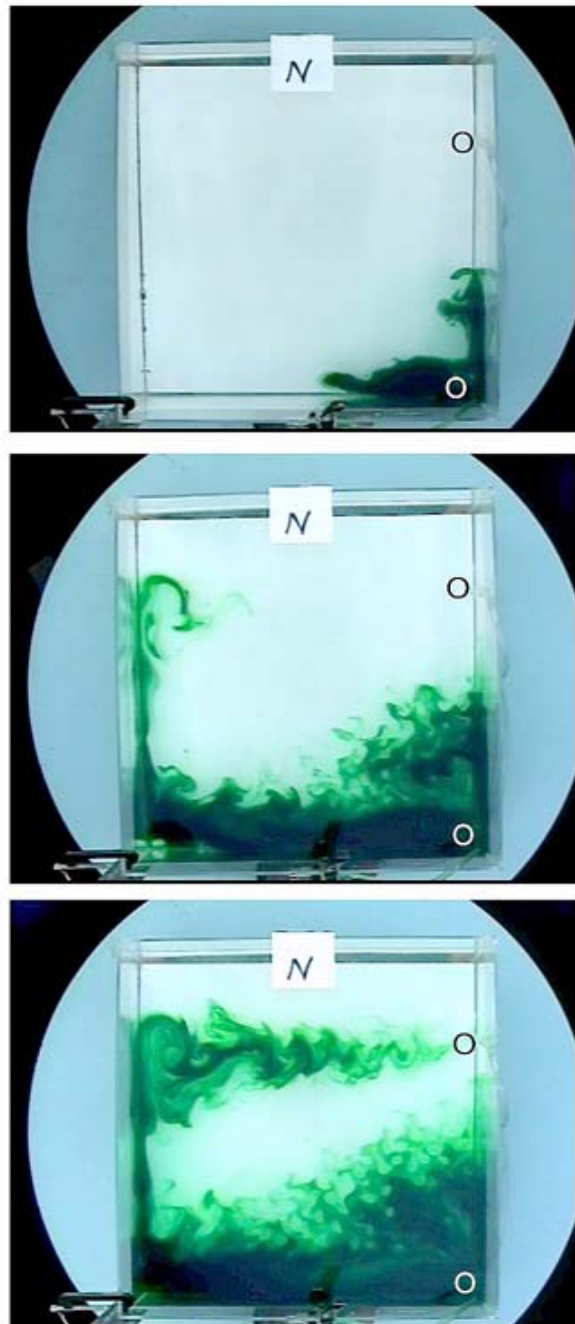


Figure 11.22: Three photographs charting the evolution of dye from source (white circle) to sink (black circle) using the apparatus shown in Fig.11.21. The shallow end of the tank is marked with the 'N' and represents polar latitudes.

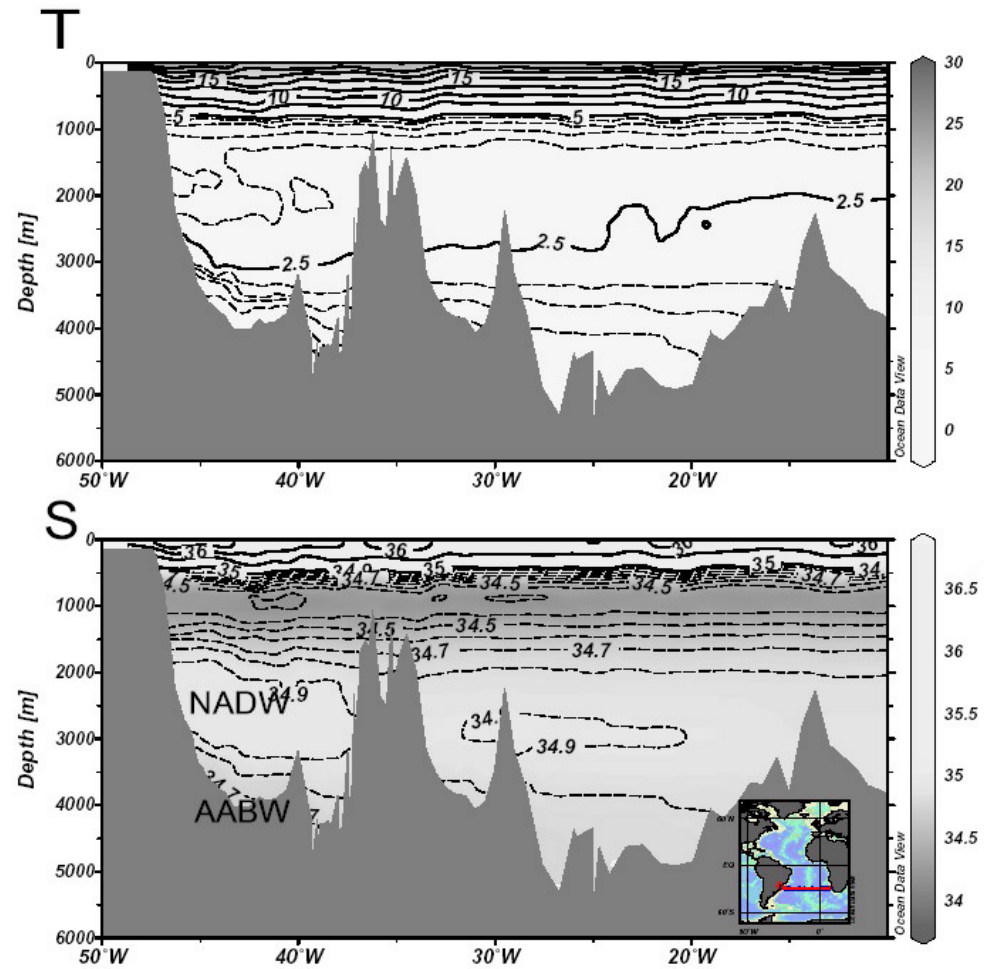


Figure 11.23: Zonal section across 30°S from the coast of South America (as marked in the inset). Top — temperature; Bottom — salinity. We see North Atlantic Deep Water flowing southwards at a depth of some 2 km and Antarctic Bottom Water moving northward right at the bottom.

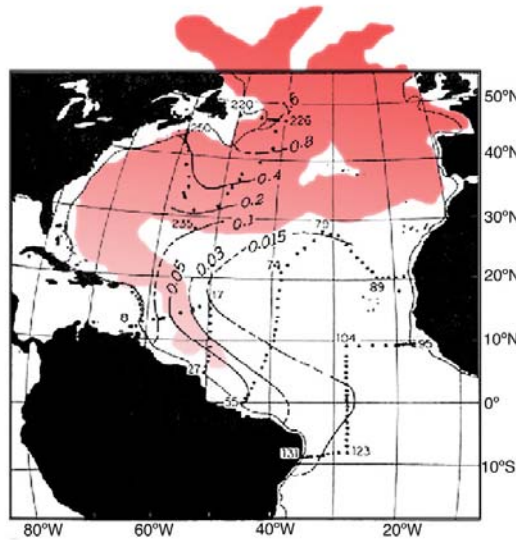


Figure 11.24: Observations of CFC's at a depth of 2 km (contoured). Superimposed in red is a snap-shot — for 1983 — of the CFC distribution at a depth of 2 km in the North Atlantic as simulated by a numerical model of ocean circulation and tracer transport. The model results are courtesy of Mick Follows (MIT), the data courtesy of Ray Weiss (Scripps).

latitudes (in the Labrador and Greenland Seas for example) CFC-enriched surface waters are mixed by convection to great depth — recall the deep mixed layers in the polar ocean shown in Fig.9.10 and 11.11 — and carried away in to the abyssal ocean by deep western boundary currents. A plume of CFC-11 can be seen in Fig.11.24 extending down the western margin of the ocean indicating the presence of a strong deep western boundary current which advects the CFC-rich waters away from the source region.

Finally, lest we leave the impression that Stommel's schematic is a detailed representation of the abyssal ocean, the gentle meridional flows sketched in Fig.11.16 are not borne out by observations. Instead, as is evident in Fig.11.25, the mid-depth flow in the ocean appears to show a marked tendency for zonal jets of small meridional scale which connect to the western boundary currents much as seen in GFD Lab XV, Fig.11.22. The lateral extent of these jets and their geographical and vertical structure are still

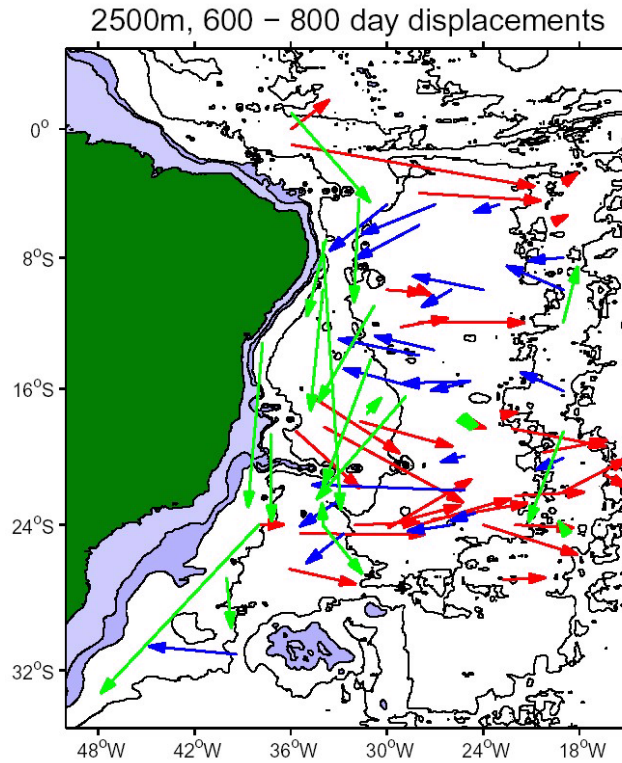


Figure 11.25: Net float displacements over periods near 600 – 800 d at a depth of 2.5 km, showing the movement of North Atlantic Deep Water in the south Atlantic. Eastward displacements are marked in red, westward in blue and southward in green. Courtesy of Nelson Hogg.

largely unknown. However, the predominantly zonal interior is consistent with the idea that there is little mixing and upwelling and so no stretching of Taylor Columns which therefore move zonally to conserve their length if not interrupted by topography.

11.5 The Ocean heat budget and transport

We now turn to the role of the ocean circulation in meridional heat transport. To maintain an approximately steady climate, the ocean and atmosphere must move excess heat from the tropics to the polar regions. We saw back

Fig.8.13 that the atmosphere transports the larger part of the poleward heat transport with the ocean carrying the remainder. To obtain a quantitative estimate of the role of the ocean in meridional heat transport we must write an equation for the ocean heat budget.

The heat budget for a column of ocean is obtained by integrating Eq.(11.2) vertically over the depth of the ocean:

$$\frac{\partial}{\partial t}(\text{heat content}) = -\mathcal{Q}_{\text{net}} - \underbrace{\nabla_h \cdot \vec{\mathcal{H}}_{\text{ocean}}}_{\text{by ocean currents}} \quad (11.11)$$

where

$$\text{heat content} = \rho_{\text{ref}} c_w \int_{\text{bottom}}^{\text{top}} T dz$$

is the heat stored in the column, \mathcal{Q}_{net} is given by Eq.(11.5) and $\vec{\mathcal{H}}_{\text{ocean}} = \rho_{\text{ref}} c_w \int_{\text{bottom}}^{\text{top}} \mathbf{u} T dz$ is the (vector) horizontal heat flux by ocean currents integrated over the vertical column and ∇_h is the horizontal divergence operator. Eq.(11.11) says that changes in heat stored in a column of the ocean are induced by fluxes of heat through the sea surface and the horizontal divergence of heat carried by ocean currents. If there is to be a steady state, the global integral of the air-sea flux must vanish (see Section 11.1) because ocean currents can only carry heat from one place to another, redistributing it around the globe.

11.5.1 Meridional heat transport

Let us define $\vec{\mathcal{H}}_{\text{ocean}}^\lambda$ as the heat flux across a vertical plane extending from the bottom of the ocean to the surface and from the western coast of an ocean basin to the eastern coast (*cf.* Eq.(8.15) for the analogous expression for the total energy flux, $\vec{\mathcal{H}}_{\text{atmos}}^\lambda$, in the atmosphere):

$$\vec{\mathcal{H}}_{\text{ocean}}^\lambda = \rho_{\text{ref}} c_w a \cos \varphi \int_{\lambda_{\text{west}}}^{\lambda_{\text{east}}} \int_{\text{bottom}}^{\text{top}} v T dz d\lambda$$

where the geometrical factor $a \cos \varphi d\lambda$ is the distance along a latitude circle over an arc $d\lambda$ (see Fig.6.19). To take account of (slight) compressibility effects, we interpret T in the above expression as the potential temperature.

$\bar{\mathcal{H}}_{ocean}^\lambda$ is difficult to measure and not precisely known. However, it can be inferred as follows:

1. as a residual, using atmospheric analyses of velocity and temperature to calculate the heat transport in the atmosphere, which is then subtracted from the total meridional transport calculated from the top-of-the-atmosphere heat flux (incoming solar minus outgoing longwave radiation) observed directly by satellite.
2. by integrating estimates of air-sea heat fluxes, such as those shown in Fig.11.4, to obtain the zonal average of the meridional heat flux (an example is shown in Fig.11.2). If a steady state prevails, the meridional integral of the zonal average of Q_{net} must be balanced by heat transport in the ocean — see Eq.(11.11) — and so yields an estimate of meridional ocean heat transport at latitude φ thus:

$$\bar{\mathcal{H}}_{ocean}^\lambda(\varphi) = -a^2 \cos \varphi \int_{\varphi_1}^{\varphi} \int_{\lambda_{west}}^{\lambda_{east}} Q_{net} d\lambda d\varphi \quad (11.12)$$

where the latitude φ_1 is chosen so that $\bar{\mathcal{H}}_{ocean}^\lambda(\varphi_1) = 0$. Eq.(11.12) simply says that in the steady state the heat flux through the sea surface integrated over an area bounded by two latitude circles and meridional coasts, must be balanced by a horizontal heat flux in to (or out of) the region, as depicted in Fig.11.26. Essentially this is how the oceanographic contribution to Fig.8.13 was computed. Note that if $Q_{net} < 0$, then $\bar{\mathcal{H}}_{ocean}^\lambda > 0$, as drawn in Fig.11.26.

3. by attempting to directly measure $\bar{\mathcal{H}}_{ocean}^\lambda$ from *in-situ* ocean observations making use of hydrographic sections such as Fig.11.23.

In Fig.11.27 we show estimates of $\bar{\mathcal{H}}_{ocean}^\lambda$ for the world ocean and by ocean basin, computed as a residual using method 1 (note the error bars can reach $\frac{1}{2}\text{PW}$). The total peaks at about $\pm 2\text{PW}$ at $\pm 20^\circ$ with the magnitude of the northward flux in the northern hemisphere exceeding, somewhat, the southward flux in the southern hemisphere. In the northern hemisphere, both the Atlantic and Pacific oceans make large contributions. In the southern hemisphere, heat is transported poleward by the Pacific and Indian Oceans, but *equatorward* by the Atlantic!

Fig.11.27 suggests that:

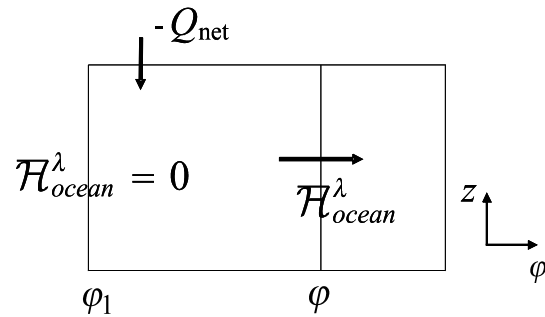


Figure 11.26: Schematic of the computation of meridional ocean heat transport from net air-sea heat flux, Eq.(11.12). The sea surface is at the top, the ocean bottom at the bottom. At the latitude φ_1 it is supposed that the meridional heat flux vanishes.

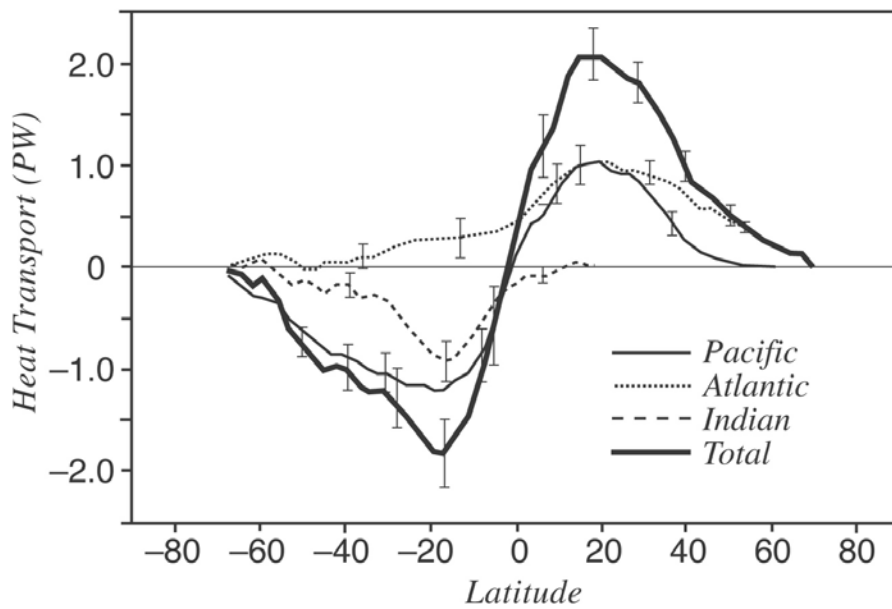


Figure 11.27: Northward heat transport in the world ocean, $\overline{\mathcal{H}}_{ocean}^\lambda$, and by ocean basin calculated by the residual method using atmospheric heat transport from ECMWF and top of the atmosphere heat fluxes from the Earth Radiation Budget Experiment satellite. The vertical bars are estimates of uncertainty. From Houghton et al. (1996) using data from Trenberth and Solomon (1994).

1. the overall magnitude of $\bar{\mathcal{H}}_{ocean}^\lambda$ is a significant fraction (perhaps $\frac{1}{4}$ to $\frac{1}{3}$) of the pole-equator heat transport (see Section 11.5.2 below) but
2. the three major ocean basins — the Atlantic, the Pacific and the Indian Ocean — differ fundamentally in their contribution to $\bar{\mathcal{H}}_{ocean}^\lambda$.

In the Pacific, the heat flux is symmetric about the equator and directed poleward in both hemispheres. In the Indian Ocean (which does not exist north of 25°N) the heat transport is southwards on both sides of the equator. In the Atlantic, however, the heat transport is northward everywhere, implying that in the south Atlantic heat is transported equatorward, up the large-scale temperature gradient. Remarkably, in the Atlantic there is a cross-equatorial heat transport of about 0.5PW (cf. Fig.8.13) and convergence of heat transport in the North Atlantic. Indeed poleward of 40°N the Atlantic ocean is much warmer (by as much as 3 °C) than the Pacific (see the map of sea-surface temperature in Fig.9.3).

Why are heat transports and SST so different in the Atlantic and Pacific sectors? It is thought to be a consequence of the presence of a vigorous overturning circulation in the Atlantic which is largely absent in the Pacific. To see this consider Fig.11.28(top) which presents a quantitative estimate of the circulation of the global ocean separated into 3 layers: shallow (top km), deep (2 to 4 km) and bottom (> 4 km). The arrows represent the horizontal volume transport (in Sv) in each of the layers across the sections marked. The circles indicate (\odot for upwelling, \otimes for downwelling) the vertical transport out of the layer in question marked in Sv . Thus, for example, $15Sv$ of fluid sinks out of the shallow layer in the northern north Atlantic: $23Sv$ of fluid travel south in the deep layer across $25S$ in the Atlantic ocean. Around Antarctica $21Sv$ of deep water upwells to the shallow layer, whilst $8Sv$ sinks in to the bottom layer. We see that the Antarctic Circumpolar Current carries a zonal transport of around $140Sv$, evenly distributed between the layers. Note the much weaker overturning circulation in the Pacific with no sinking of fluid in the northern North Pacific.

Fig.11.28(bottom) is a gross, but useful, cartoon of the upper branch (shallow to deep) overturning circulation highlighting the asymmetry between the Atlantic and the Pacific and between the northern and southern hemispheres⁶. We see that a major pathway accomplishing northward

⁶This schematic representation has been dubbed the ‘conveyor belt’ both in scientific and popular articles.

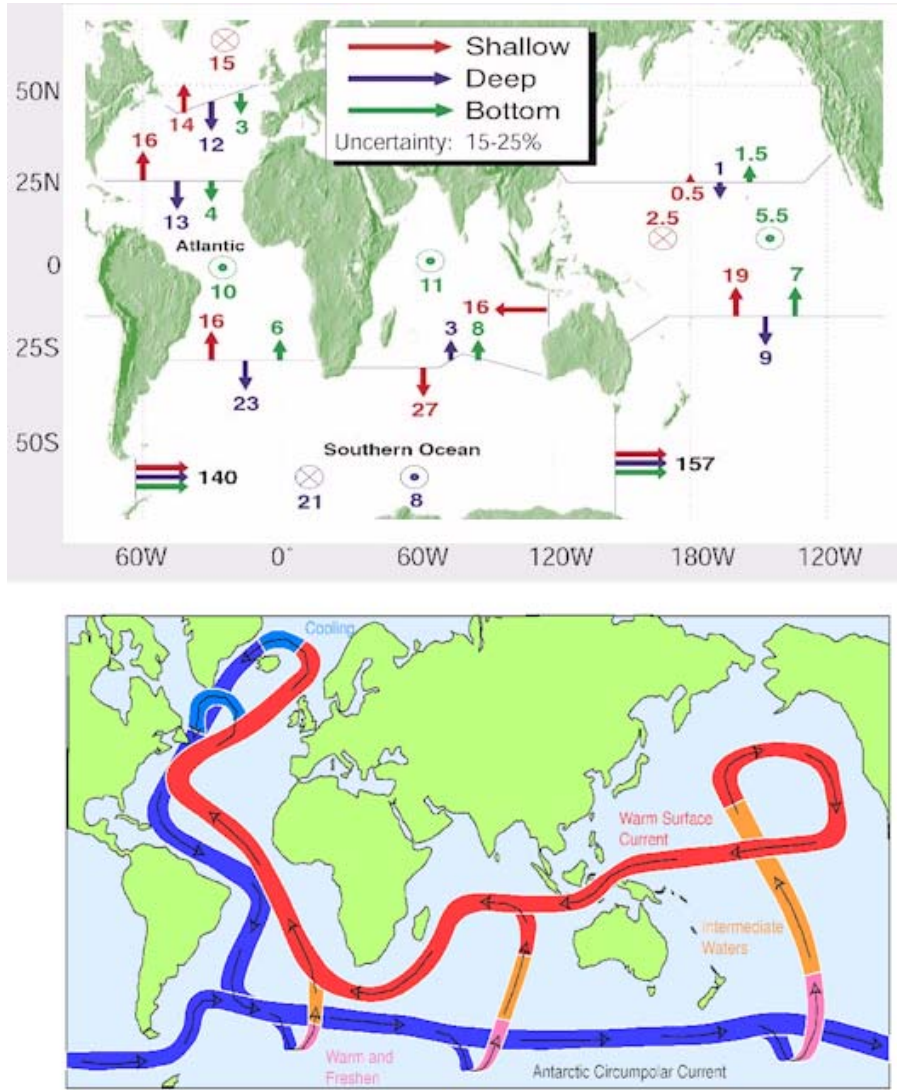


Figure 11.28: (top) Estimates of global ocean circulation patterns based on Ganachaud & Wunsch (2000) published in Alley et al., 2002. (bottom) A cartoon of the ocean's shallow to deep global meridional overturning circulation proposed by David Webb (Southampton Oceanography Center) illustrating the asymmetry between the Atlantic and Pacific basins and between northern and southern hemispheres.

heat transport in the Atlantic is the advection of warm, near-surface water northward across the equator (see the northward flowing western boundary current crossing the equator in Fig.10.13, bottom), cooling and sinking in the northern north Atlantic and thence southwards flow of colder fluid as North Atlantic Deep Water. In contrast, the Pacific ocean does not support a significant overturning cell induced by polar sinking. This is the key to understanding the different nature of heat transport in the basins evident in Fig.11.27.

11.5.2 Mechanisms of ocean heat transport and the partition of heat transport between the atmosphere and ocean

Heat is transported poleward by the ocean if, on the average, waters moving polewards are compensated by equatorward flow at colder temperatures. It is useful to imagine integrating the complex 3-dimensional ocean circulation horizontally, from one coast to the other, thus mapping it out in a meridional plane, as sketched in Fig.11.29. If surface waters moving poleward are warmer than the equatorial return flow beneath, then a poleward flux of heat will be achieved.

To make our discussion more quantitative we write down the meridional advection of heat thus (integration across the ocean is implied):

$$\begin{aligned}
 \mathcal{H}_{ocean} &= c_w \int_{bottom}^{top} \rho_{ref} v \vartheta dz \\
 &= -c_w \int_{bottom}^{top} \frac{\partial \Psi_O}{\partial z} \vartheta dz = c_w \int_{bottom}^{top} \Psi_O \frac{\partial \vartheta}{\partial z} dz \\
 &= c_w \int_{\vartheta_{bottom}}^{\vartheta_{top}} \Psi_O d\vartheta.
 \end{aligned} \tag{11.13}$$

In deriving the above we have written $\rho_{ref}v = -\frac{\partial \Psi_O}{\partial z}$ in which Ψ_O is the streamfunction for the mass transport in the meridional plane and made use of the fact that $\Psi_O = 0$ at the top and bottom of the ocean and that the mass transport can be expressed as the product of the density of water multiplied by the volume transport of the meridional overturning circulation (MOC), ψ_{MOC} thus:

$$\Psi_O = \rho_{ref} \psi_{MOC}. \quad (11.14)$$

The relation $\mathcal{H}_{ocean} = c_w \int_{\vartheta_{bottom}}^{\vartheta_{top}} \Psi_O d\vartheta$ tells us that the heat transport can be expressed in terms of the mass transport in temperature layers, or, more generally, noting the multiplication by c_w , the mass transport in energy layers. It is then useful to write down an approximate form thus:

$$\mathcal{H}_{ocean} \simeq c_w \Delta\vartheta \Psi_{O_{max}} \quad (11.15)$$

where $\Delta\vartheta$ is the difference in potential temperature between the poleward and equatorward branches and $\Psi_{O_{max}}$ is the strength of the overturning mass transport.

Fig.11.30 shows ψ_{MOC} for the North Atlantic⁷: we see that it has a magnitude of order 20Sv, implying a meridional mass transport of $\Psi_{O_{max}} = 12 \times 10^9 \text{ kg s}^{-1}$. If the temperature difference across the MOC is $\Delta\vartheta = 15 \text{ K}$, typical of the temperature drop across the main thermocline (see Fig.9.5) then Eq.(11.15) yields a heat transport of 0.5PW, of the order presented in Fig.11.27. Thus Eq.(11.15) is a useful vantage point from which to discuss mechanisms of ocean heat transport and — see below — the partition of heat transport between the atmosphere and the ocean.

Both wind-driven and thermohaline circulations play an important role in setting the magnitude and pattern of Ψ_O . Fluid which is pumped down by the wind in middle latitudes is compensated in part by poleward transport of warm surface waters from the tropics in surface Ekman layers. The subsurface equatorial return flow occurs at a colder temperature, resulting in poleward heat transport. This is a primary mechanism of heat transport in, for example, the Pacific ocean, where wind-driven circulations dominate resulting in a transport which is symmetric about the equator (see Fig.11.27). In the Atlantic, however, a convectively-induced (thermohaline) component is superimposed and intimately intertwined with wind-driven processes. Here the ocean heat transport is northward at all latitudes, consistent with the idea that a giant inter-hemispheric meridional overturning cell associated with polar sinking is a dominant heat transport mechanism, as sketched in Fig.11.28(bottom). As we shall discuss in more detail in Section 12.3.5, variability in the MOC in the Atlantic ocean is often invoked as a player of climate

⁷The overturning circulation shown in Fig.11.30 is derived from a model constrained by observations, rather than inferred directly from observations, because it is all but impossible to observe ψ_{MOC} directly.

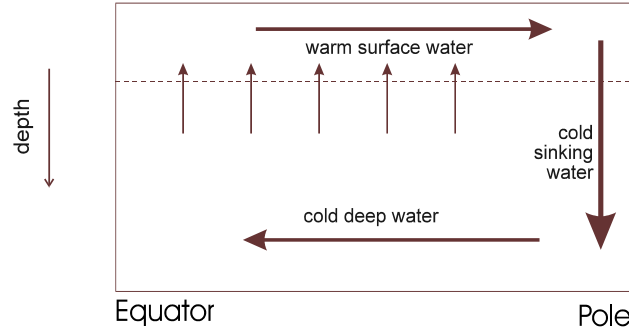


Figure 11.29: A schematic diagram of the ocean's meridional overturning circulation, in which warm waters flow poleward at the surface, are cooled by loss of heat to the atmosphere, sink to depth and return equatorward. Such a circulation achieves a poleward transport of heat.

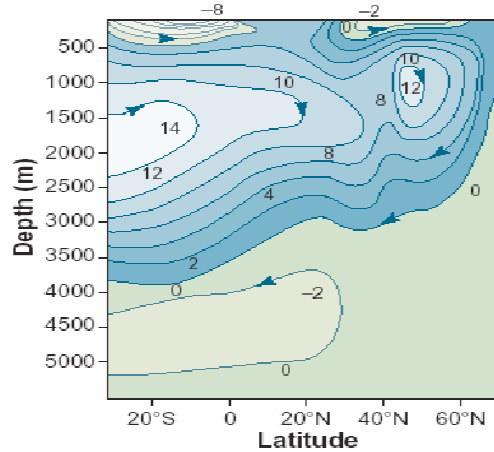


Figure 11.30: The meridional overturning circulation, ψ_{MOC} , in a model of the the Atlantic ocean showing inter-hemispheric circulation. The units are in Sv. From Wunsch, 2002.

change because of the likely sensitivity of Arctic processes to meridional heat transport mediated by the MOC.

The framework provided by Eq.(11.15) can also be used to come to some understanding of the processes that set the partition of heat transport between the atmosphere and ocean. We can express the atmospheric heat transport in the same form:

$$\mathcal{H}_{atmos} \simeq c_p \Delta\vartheta_A \Psi_{A_{max}} \quad (11.16)$$

where now $\Psi_{A_{max}}$ is the magnitude of the mass transport overturning circulation of the atmosphere in “energy” layers, appropriately chosen based on moist static energy such that

$$c_p \Delta\vartheta_A = c_p \Delta T + g \Delta z + L \Delta q$$

is the vertical change in the moist static energy (see Eq.(8.16) and the discussion of meridional transport of heat in Section 8.4) across the overturning circulation.

In Fig.11.31 we plot annual-mean mass transport streamfunction for the atmosphere and ocean, Ψ_A and Ψ_O , in energy layers, $c_p \Delta\vartheta_A$ for the atmosphere and $c_w \Delta\vartheta_O$ for the ocean. The horizontal axis is latitude, the vertical axis is an energy coordinate with units of $c\Delta\vartheta$, i.e. $J\text{kg}^{-1}$. To facilitate comparison of the strength of the overturning circulation in the two fluids, we have (temporarily) redefined the Sverdrup as an equivalent unit of mass transport: in Fig.11.31 1 Sv is the mass transport associated with a volume flux of $10^6 \text{ m}^3 \text{s}^{-1}$ of water — i.e. $10^6 \text{ m}^3 \text{s}^{-1} \times 10^3 \text{ kg m}^{-3} = 10^9 \text{ kg s}^{-1}$. The first striking feature of Fig.11.31 is that, in contrast to Fig.5.21, the atmospheric overturning circulation comprises one giant cell from equator to pole. This is because, unlike the overturning circulation plotted in Fig.5.21, Fig.11.31 includes a large eddy contribution: in middle-to-high latitudes, mass (like heat) is transferred by weather systems rather than by the mean flow. Secondly, note that the intensity of the oceanic cell is much weaker than its atmospheric counterpart. Even at 20° , where Ψ_O reaches its maximum, the atmospheric mass transport is roughly four times that of the ocean. It is only within the deep tropics that the two transports are comparable. The third important feature is that the ‘thickness’ of the overturning cells in the two fluids are comparable in energy space. In midlatitudes, $c_w \Delta\vartheta_O / c_p \Delta\vartheta_A$ is of order unity, the differences in heat capacity ($c_w/c_p \sim 4$) being compensated by a larger temperature difference across the atmospheric cell ($\Delta\vartheta_A \sim$

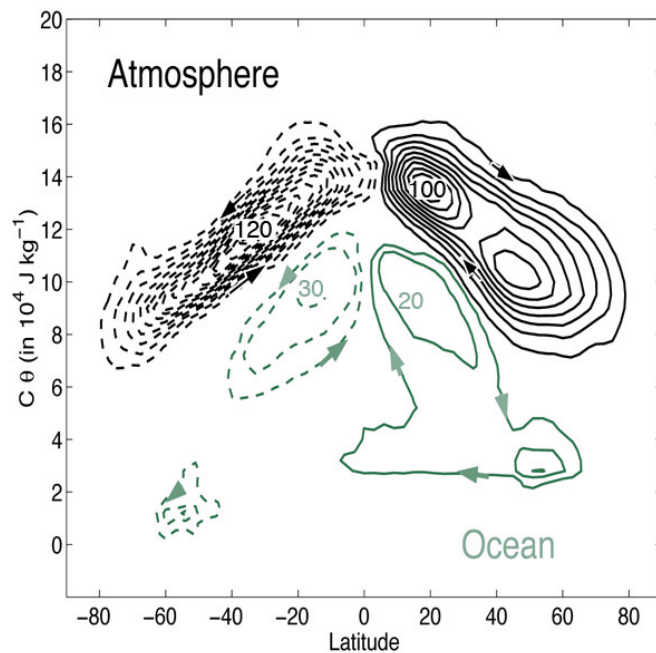


Figure 11.31: Annual mean atmospheric (black) and oceanic (green) mass streamfunction within constant energy layers. The contour interval is $10Sv$ where $1Sv = 10^9 \text{ kg s}^{-1}$, dashed when circulating anti-clockwise. The horizontal axis is latitude; the vertical axis is an energy coordinate ($c\Delta\vartheta$) in units of 10^4 J kg^{-1} . From Czaja and Marshall (2006).

$40K$ compared to $\Delta\vartheta_O \sim 10K$). The dominance of atmospheric over ocean heat transport in middle-to-high latitudes can thus be rationalized as being a consequence of Ψ_A greatly exceeding Ψ_O (see Fig.11.31).⁸ Finally, note that Ψ_O is dominated by two large symmetrically disposed cells around the equator — this, in the main, is the overturning cell associated with wind-driven subtropical gyres, carrying heat up to 40° N, S or so. The weaker cells at lower temperatures in polar latitudes are the signature of overturning cells directly associated with convectively-induced, polar thermohaline circulations.

11.6 Freshwater transport by the ocean

The ocean and atmosphere must move freshwater from regions of excess rainfall to regions with excess evaporation — see Fig.11.6. Knowledge of water fluxes and transports in the ocean is important for understanding the global hydrological cycle and climate. For example, variability in fresh water fluxes may have played an important role in the ice ages, as will be discussed in Chapter 12. The plot of evaporation minus precipitation shown in Fig.11.6 shows that evaporation exceeds precipitation by more than a meter per year in the trade wind regimes in the eastern parts of the oceans. Here dry air subsides along the poleward edges of the Hadley Cell. The ITCZ is a region of vigorous updrafts and here precipitation exceeds evaporation. As discussed in Chapter 9, these broad patterns of E and P are reflected in the surface salinity distribution of the oceans (see Fig.9.4).

The transport of fresh water by the ocean can be calculated using the same methods as for heat transport — again there is considerable uncertainty in these estimates. Fig.11.32 shows an estimate of the meridional transport of freshwater by the Atlantic Ocean. We see that freshwater transport is southwards, corresponding to a transport of saltwater northwards into the North Atlantic. This salinization is thought to play an important role in preconditioning the surface waters of the Atlantic to convection when exposed to cooling in polar latitudes.

⁸It is remarkable that despite the density of air being typically one thousand times less than that of water, the meridional mass transport in the atmosphere ($\sim 100\text{Sv} = 10^{11}\text{ kg s}^{-1}$) exceeds that of the ocean by a factor of 4. This is because meridional wind speeds greatly exceed those in the ocean.

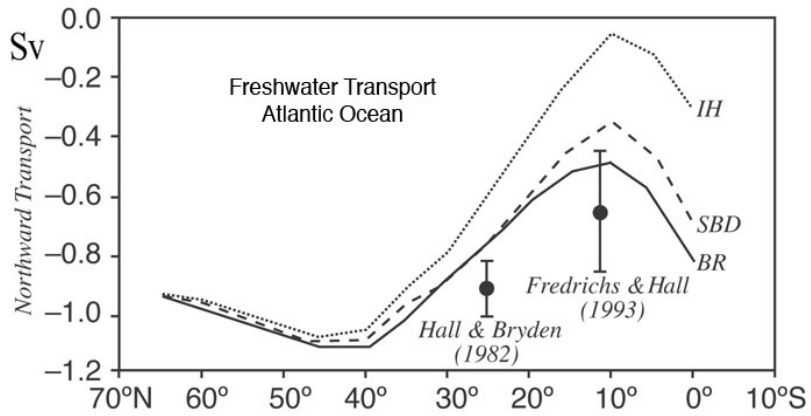


Figure 11.32: Meridional transport of fresh water by the Atlantic from three surface-flux calculations: BR-Baumgartner and Reichel (1975); SBD-Schmitt et al. (1989); and IH - Isemer and Hasse's (1987) evaporation estimates combined with Dorman and Bourke's (1981) precipitation values. Also shown are direct measurements at 24°N by Hall and Bryden (1982) and 11°N by Friedrichs and Hall (1993). All are summed relative to an estimated Arctic southward export due to the Bering Strait through flow and the water budget of the Arctic itself. From Schmitt (1994) and Stewart (1995).

11.7 Further reading

A more comprehensive discussion of air-sea interaction can be found in Csanady (2001) and Stewart (2003). Dynamical theories of thermohaline circulation are less well developed than those of the wind-driven ocean circulation. Good accounts of Stommel's theory of abyssal ocean circulation can be found in Pedlosky (1996) and Vallis (2006).

11.8 Problems

1. It is observed that water sinks in to the deep ocean in polar regions of the Atlantic basin at a rate of $15Sv$.
 - (a) How long would it take to 'fill up' the Atlantic basin?
 - (b) Supposing that the local sinking is balanced by large-scale upwelling, estimate the strength of this upwelling. Express your answer in $m\text{ y}^{-1}$.
 - (c) Assuming that $\beta v = f \frac{\partial w}{\partial z}$, infer the sense and deduce the magnitude of the meridional currents in the interior of the abyssal ocean where columns of fluid are being stretched.
 - (d) Estimate the strength of the western boundary current.
2. Review Section 11.3.3, but now suppose that boundary currents flow northwards in Fig.11.20. By considering the role of boundary current friction in inducing Taylor columns to stretch/compress — Eq.(11.10) — deduce that northward flowing eastern (western) boundary currents are disallowed (allowed).
3. Consider the laboratory experiment GFD XV — source sink flow in a rotating basin. Use the Taylor-Proudman theorem and that eastern boundary currents are disallowed, to sketch the pattern of flow taking fluid from source to sink for the scenarios given in Fig.11.33. Note that one of the solutions is given in Fig.11.22!
4. From Fig.11.6 one sees that evaporation exceeds precipitation by order 1 m y^{-1} in the subtropics ($\pm 30^\circ$), but the reverse is true at higher latitudes ($\pm 60^\circ$).

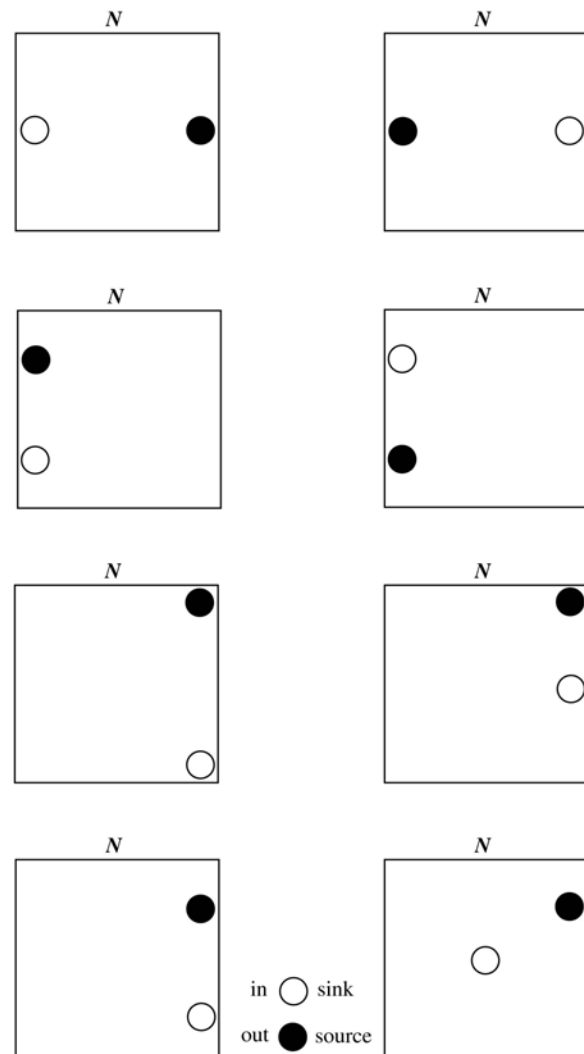


Figure 11.33: Possible placement of the source and sink in GFD LabXV — source sink flow in a rotating basin. Note that Fig.11.22 corresponds to the case at the bottom of the column on the left.

- (a) Estimate the meridional freshwater transport of the ocean required to maintain hydrological balance and compare with Fig.11.32.
 - (b) Latent heat is taken from the ocean to evaporate water which subsequently falls as rain at (predominantly) higher latitudes, as sketched in Fig.11.5. Given that the latent heat of evaporation of water is $2.25 \times 10^6 \text{ J kg}^{-1}$, estimate the implied meridional flux of energy in the atmosphere and compare with Fig.8.13.
5. In the present climate the volume of freshwater trapped in ice sheets over land is $\sim 33 \times 10^6 \text{ km}^3$. If all this ice melted and ran into the ocean, by making use of the data in Table 9.1, estimate by how much the sea level would rise. What would happen to sea level if all the sea-ice melted?

